Recharacterization of RSL3 reveals that the selenoproteome is a druggable target in colorectal cancer

Stephen L. DeAngelo[1,2,12], Sofia Dziechciarz[2], Sumeet Solanki[2], Myungsun Shin[3,4], Liang Zhao[2], Andrii Balia[6], Marwa O El-Derany[2,5], Nupur K Das[2], Cristina Castillo[2], Hannah N Bell[2], Joao A. Paulo[3,4], Yuezhong Zhang[2], Nicholas J Rossiter[2,12], Elizabeth C. McCulla[1,12], Jianping He[7], Indrani Talukder[2], Zachary T. Schafer[7], Nouri Neamati[5,12], Joseph D. Mancias[4,8], Markos Koutmos[9,10,*], Yatrik M. Shah[2,11,12,*]

Affiliations:

[1]Doctoral Program in Cancer Biology, University of Michigan Medical School, Ann Arbor, MI, United States
[2]Department of Molecular and Integrative Physiology, University of Michigan, Ann Arbor, MI, United States
[3]Department of Cell Biology, Harvard Medical School, Boston, MA, United States
[4]Dana-Farber Cancer Institute, Boston, Massachusetts, United States
[5]Department of Biochemistry, Faculty of Pharmacy, Ain Shams University, Cairo, Egypt.
[6]Department of Medicinal Chemistry, College of Pharmacy, University of Michigan, Ann Arbor, Michigan, United States
[7]Department of Biological Sciences, University of Notre Dame, Notre Dame, IN, United States
[8]Division of Radiation and Genome Stability, Department of Radiation Oncology, Dana-Farber Cancer Institute, Harvard Medical School, Boston, MA. United States
[9]Department of Chemistry, University of Michigan, Ann Arbor, MI, United States
[10]Department of Biophysics, University of Michigan, Ann Arbor, MI, United States
[11]Department of Internal Medicine, University of Michigan, Ann Arbor, MI, United States
[12]Rogel Cancer Center, University of Michigan, Ann Arbor, MI, United States

*Corresponding: mkoutmos@umich.edu, shahy@umich.edu

Abstract
Ferroptosis is an iron-dependent, non-apoptotic form of cell death resulting from the accumulation of lipid peroxides. Colorectal cancer (CRC) accumulates high levels of intracellular iron and reactive oxygen species (ROS), thereby sensitizing cells to ferroptosis. The selenoprotein glutathione peroxidase (GPx4) is a key enzyme in the detoxification of lipid peroxides and can be inhibited by the compound (S)-RSL3 ([1S,3R]-RSL3). However, the stereoisomer (R)-RSL3 ([1R,3R]-RSL3), which does not inhibit GPx4, exhibits equipotent activity to (S)-RSL3 across a panel of CRC cell lines. Utilizing CRC cell lines with an inducible knockdown of GPx4, we demonstrate that (S)-RSL3 sensitivity does not align with GPx4 dependency. Subsequently, a biotinylated (S)-RSL3 was then synthesized to perform affinity purification-mass spectrometry (AP-MS), revealing that (S)-RSL3 acts as a pan-inhibitor of the selenoproteome, targeting both the glutathione and thioredoxin peroxidase systems as well as multiple additional selenoproteins. To investigate the therapeutic potential of broadly disrupting the selenoproteome as a therapeutic strategy in CRC, we employed further chemical and genetic approaches to disrupt selenoprotein function. The findings demonstrate that the selenoprotein inhibitor Auranofin can induce ferroptosis and/or oxidative cell death both *in-vitro* and *in-vivo*. Consistent with this data we observe that AlkBH8, a tRNA-selenocysteine methyltransferase required for the translational incorporation of selenocysteine, is essential for CRC growth. In summary, our research elucidates the complex mechanisms underlying ferroptosis in CRC and reveals that modulation of the selenoproteome provides multiple new therapeutic targets and opportunities in CRC.

Introduction

Colorectal Cancer (CRC) is the fourth most common cancer and fifth leading cause of cancer related deaths in the US[1]. Most early CRC is found through routine colonoscopies and if found early, CRC is curable with surgical resection and adjuvant chemotherapy[2]. However, recent data demonstrate a concerning rise in the incidence rate of CRC in young adults whom often present with advanced disease[3]. Metastatic CRC is incurable and is commonly driven by inactivating mutations of the tumor suppressor genes APC and TP53, leaving minimal opportunities for the development of targeted therapeutics[4,5]. While recent advances in immunotherapy have demonstrated remarkable success in mismatch repair deficient (MMR) CRC[6], only a small subset of CRC patients are diagnosed with MMR CRC[7], limiting its widespread utility. Therefore, new effective therapies for CRC are desperately needed.

CRCs are highly iron addicted and an emerging strategy for the treatment of CRC is the iron-dependent, non-apoptotic form of cell death, ferroptosis[8]. In the presence of labile iron, intracellular hydrogen peroxide undergoes radical decomposition into a hydroxyl ion and a hydroxyl radical, a process known as the Fenton reaction[9]. The hydroxyl radical then rapidly proliferates through the cell, causing widespread DNA, protein, and lipid peroxidation. The accumulation of lipid peroxides is a key characteristic of ferroptosis and results in membrane instability leading to cell rupture[10]. However, in contrast to apoptosis, ferroptosis lacks distinct, well-defined markers for its characterization[11]. Therefore, the main distinguishing characteristic of ferroptosis is its ability to be rescued by the lipid reactive oxygen species (ROS) scavenging antioxidants liproxstatin-1 and ferrostatin-1[12].

Glutathione peroxidase (GPx)4 utilizes reduced glutathione (GSH) to directly detoxify lipid ROS, leading to characterization of GPx4 as a central regulator of ferroptosis[13]. Central to the activity of GPx4 is a catalytic selenocysteine residue as GPx4 is a selenoprotein – one of 25 proteins in the human genome that selectively incorporate selenocysteine[14–16] – known collectively as the selenoproteome. In these enzymes, the selenocysteine is essential for catalytic function as selenocysteine to cysteine point mutations in GPx4 result in >90% loss of activity, albeit supraphysiological overexpression of this reduced activity mutant can still rescue ferroptosis induction *in-vitro*[17]. The discovery of Ras-Sensitive Ligand 3 (RSL3), identified as a GPx4 inhibitor[13], has further cemented the characterization of GPx4 as the central regulator of ferroptosis[18]. While there is broad cell line sensitivity to RSL3, this does not always correlate with GPx4 expression, casting doubt on RSL3 as a specific inhibitor of GPx4. Through the

generation of doxycycline-inducible GPx4 knockdown cell lines (GPx4 i-KD), we identified a CRC cell line (DLD1) that is sensitive to RSL3 but insensitive to GPx4 i-KD. Through synthesis of biotinylated RSL3, we then performed streptavidin-based affinity pulldown of CRC lysates to identify RSL3 targets by tandem-mass tag (TMT) quantitative proteomics. Our data reveals that RSL3 has numerous targets and is a non-specific inhibitor of the selenoproteome and thioredoxin peroxidases, including the selenoprotein Thioredoxin Reductase 1. We then undertook chemical and genetic approaches to inhibit the selenoproteome. In our studies we demonstrate that the selenoproteome is essential for the growth and survival of CRC cell lines in *in-vitro* and *in-vivo* models, thus characterizing broad inhibition of selenoproteins as a novel therapeutic strategy in CRC.

Methods

Mice

All mice used in these studies are from either a Balb/c or C57Bl/6J background. Males and females are equally represented, and littermates were randomly mixed in all experimental conditions. The mice were housed in a temperature controlled, specific pathogen free environment, with a 12-hour light/dark cycle. They were fed *ad-libitum* with either a standard chow diet or auranofin dosed diet as indicated. Mice were between 6 and 8 weeks old at study initiation. All animal studies were carried out in accordance with the Association for Assessment and Accreditation of Laboratory Animal Care International guidelines and approved by the University Committee on the Use and Care of Animals at the University of Michigan.

Human Survival Analysis

Human survival analysis was determined using the online tool KMplot[19]. This is a web-based, registration-free survival analysis tool that can perform univariate and multivariate survival analysis. Significance is computed using the Cox-Mantel log-rank test.

Human Normal vs Tumor Gene Expression Analysis

Human normal vs. tumor gene expression analysis was determined using the online tool UALCAN (University of Alabama at Birmingham Cancer Data Analysis Portal)[20,21]. This is a web-based, registration-free gene expression analysis tool for the analysis of cancer OMICS data from the TCGA (The Cancer Genome Atlas Project).

Cell lines

Human colorectal carcinoma cell lines HCT116, RKO, SW480, and DLD1 were used for most experiments. Mouse colorectal carcinoma cell lines MC38 and CT26, as well as the human normal intestinal cell line NCM460 were also used. Cell lines have been STR-authenticated and routinely tested for mycoplasma contamination by PCR. All cells were maintained in complete DMEM medium (supplemented with 10% fetal bovine serum and 1% antibiotic/antimycotic agent) at 37 °C in 5% CO_2 and 21% O_2. Cell numbers were quantified for plating and xenograft experiments using a Multisizer 4e Coulter Counter (Beckman-Coulter).

Growth assays

Adherent cell growth assays were performed via label free live cell imaging using the Cytation 5 Imaging Multi-Mode reader with attached BioSpa (Agilent BioTek). For 72 hr growth analysis cells were plated at ~500 cells/well while for 144 hr growth analysis cells were plated at ~100 cells/well. Cells were allowed to adhere overnight, imaged and analyzed for cell number at t_0, and then immediately treated as indicated in the figure legend; images were then acquired every 8-24 hr as indicated. Cytation software was used to quantify adherent cell counts. Analysis was performed by normalization to cell number at first reading (0 hr), with a minimum of 3 independent wells averaged for statistical analysis. Graphs were plotted using Prism with error bars representing mean +/- standard deviation. Growth assay data was utilized for the generation and calculation of EC_{50} curves. The average fold change at the endpoint of an untreated control group (minimum of 3 replicates) was normalized to a value of 1.0 and the relative fold change of treated wells (minimum 3 replicates per group) was then calculated as a fractional response as compared to the average of the untreated control. EC_{50} values were determined using Prism sigmoidal standard curve interpolation. Statistical significance was determined using Prism 2-way ANOVA with multiple comparisons.

Clonogenic Assays (Colony Formation Assays)

Cells were plated in biological triplicates in a 6-well plate at 500 cells per well in 3 mL of media. Cells were treated as indicated in the figure legends with media and treatment replenished every 5 days. Assays were concluded at 12-15 days by fixing cells in cold 10% buffered formalin for 10 min and staining with 1% crystal violet, and 10% methanol solution for 30 min. Colony plates were washed in dH_2O and imaged using an iBright FL1500 imaging system (Thermo Fisher)

Histology and 4-HNE staining.

Colonic tissues or tumor tissues were rolled and fixed with PBS-buffered formalin for 24 hours then transferred to 70% ethanol, followed by embedding in paraffin. Sections of 5 µm were stained for H&E and mounted with Permount Mounting Medium (Thermo Fisher Scientific). For 4-hydroxy-2-noneal/4-HNE staining, paraffin-embedded tissue sections were subjected to antigen retrieval, followed by blocking with 5% goat serum in PBS, and probed with primary antibody against 4-HNE (1:200 dilutions, BS6313R, Bioss). Sections were then washed 3 times with PBST and were incubated with HRP-conjugated anti-rabbit IgG (1:500 dilution, catalog 7074S, Cell Signaling Technology) for 1 hr. Sections were then washed 3 times with PBST and incubated with DAB substrate solution to sufficiently cover them. After the sample color turned

brown, the reaction was stopped by distilled water, and dehydration steps commenced. The slides were mounted using Permount Mounting Medium (Fischer).

Western Blotting.

Indicated cells were seeded in a 6-well plate in triplicate for each condition and allowed to adhere overnight. Cells were plated to reach ~$0.8x10^6$ cells/well at time of harvest. Cells were lysed with RIPA assay buffer with added protease (1:100 dilution; MilliporeSigma) and phosphatase (1:100 dilution; Thermo Fisher Scientific) inhibitors. Lysates were quantified by BCA protein assay kit (Pierce – Thermo Fisher Scientific) and normalized for loading. Solubilized proteins were resolved on 10% SDS-polyacrylamide gels and transferred to nitrocellulose membrane, blocked with 5% milk in TBST, and immunoblotted with the indicated primary antibodies: GPx4 monoclonal (Proteintech 67763-1-Ig), TxnRD1 (Santa Cruz sc-28321), Actin (Proteintech 66009-1-Ig). HRP-conjugated secondary antibodies used were anti-rabbit and anti-mouse at a dilution of 1:2000 and immunoblots were developed using Chemidoc imaging system (ChemiDoc, BioRad).

qPCR

Cell lines were treated for indicated times (typically 72 hrs) and washed with sterile PBS prior to RNA extraction with Trizol reagent. Total RNA was visualized on an agarose gel to confirm high quality extraction, with RNA yield quantified using a Nanodrop. 1µg of total RNA was reverse transcribed to cDNA using SuperScriptTM III First-Strand Synthesis System (Invitrogen). Real time PCR reactions were set up in three technical replicates for each sample. cDNA gene specific primers and SYBR green master mix were combined and then run in QuantStudio 5 Real-Time PCR System (Applied BioSystems). The fold-change of the genes were calculated using the ΔΔCt method using *Actb* as the housekeeping mRNA. qPCR primers used:
Actin F: CACCATTGGCAATGAGCGGTTC. Actin R: AGGTCTTTGCGGATGTCCACGT
AlkBH8 F: AGGTCTTTGCGGATGTCCACGT AlkBH8 R: GAGAGCATCCACCAGTCCACAT

Generation of Doxycycline Inducible Cell Lines

Doxycycline inducible cell lines were generated using the pLKO.1-Tet On system[22]. shRNA sequences were cloned into the pLKO.1-Tet On backbone, sequence validated via Sanger Sequencing (Genscript), and utilized for lentivirus production through the University of Michigan Vector Core. Cells were transfected with lentiviral particles through spinfection at 900xg, 37 °C, 1 hr in the presence of polybrene (final concentration = 10 µg/mL) then incubated at 37 °C, 5% CO2 for 24 hrs. The next day media was changed and cells were allowed to recover for 24 hrs

before addition of puromycin (2 µg/mL) to the culture media. Cells were maintained in puromycin until an untreated control well demonstrated 100% cell death. shRNA sequences:
GPx4 sh2: GTGGATGAAGATCCAACCCAA
GPx4 sh3: GCACATGGTTAACCTGGACAA
AlkBH8 sh3: TTACCTGAACACATCATATAT
AlkBH8 sh4: CAGGTGGGAAGGCACTCATTT

Streptavidin-Affinity Pull Down

Streptavidin-Affinity MS was performed on isolated cell lysates. Cells were plated in 15 cm dishes in normal DMEM (10% FBS, 1% Anti-Anti) and allowed to adhere for 24 hrs. The next day cells were treated with 1 µM selenium in the form of Sodium selenite to increase translation of trace selenoproteins that may otherwise be vulnerable to dropout. Sodium selenite was prepared as a 100 mM stock in ddH_2O. 24 hrs after administration of selenium, cells were washed with sterile PBS and scraped directly into ice cold RIPA buffer. The protocol was optimized to utilize 10 mg of total lysate per biological replicate to obtain signal over the noise threshold. Soluble lysate was treated overnight at 4 °C with the EC_{50} concentration of the respective compound. The next day Streptavidin-coated magnetic beads (Vector Laboratories) were added and the mixture was incubated with gentle rocking at 4 °C for 2 hrs. Beads were then washed 3x in RIPA using a magnetic separation rack, and a further 3x in SDS-free wash buffer (50 mM Tris-HCl, pH 7.4, 150 mM NaCl, 1 mM TCEP). Beads were then pelleted via centrifugation, flash frozen in LN_2, and stored at -80 °C prior to MS processing.

LC-MS/MS

All samples were resuspended in 100 mM 4-(2-Hydroxyethyl)-1-piperazinepropanesulfonic acid (EPPS) buffer, pH 8.5, and digested at 37 °C with trypsin overnight. The samples were labeled with TMT Pro and quenched with hydroxylamine. Samples were desalted via StageTip and dried with speedvac. Samples were resuspended in 5% formic acid, and 5% acetonitrile for LC-MS/MS analysis. Mass spectrometry data were collected using an Astral mass spectrometer (Thermo Fisher Scientific) coupled with a Vanquish Neo liquid chromatograph (Thermo Fisher Scientific) with a 75 min gradient and Nano capillary column (100 µm D) packed with ~35 cm of Accucore C18 resin (Thermo Fisher Scientific). A FAIMSPro (Thermo Fisher Scientific) was utilized with -30,-35,-45,-55,-60, and -70V for field asymmetric waveform ion mobility spectrometry (FAIMS) ion separations. Data acquisition was performed with a mass range of m/z 350-1350 using a TopSpeed method of 1 s. MS1 resolution was set at 60,000 and singly-

charged ions were not sequenced. MS1 AGC target was set as standard, and the maximum ion time was set at 50 ms. For MS2 analysis in the Astral analyzer, only multi-charge state ions (z=2-5) were isolated and fragmented using an HCD collision energy of 35%, an isolation window of 0.5 Th, with a dynamic exclusion of 15 s. MS2 AGC target was set as standard, and the maximum ion time was set at 20ms.

Raw files were searched using the Comet algorithm with a custom database search engine reported previously[23]. Database searching included human (*Homo Sapiens*) entries from UniProt (http://www.uniprot.org, downloaded 2021) with the reversed sequences, and common contaminants (i.e., keratins, trypsin). Peptides were searched using the following parameters: 50 ppm precursor mass tolerance; up to 2 missed cleavages; variable modifications: oxidation of methionine (+15.9949); static modifications: TMTpro (+304.2071) on lysine and peptide N-terminus, carboxyamidomethylation (+57.0215) on cysteines and selenocysteines. The protein-level FDR was determined using the ModScore algorithm where a score of 13 corresponds to 95% confidence in correct localization. TMT reporter ions were used for quantification of peptide abundance. Isotopic impurities were corrected according to the manufacturer's specifications, and signal-to-noise (S/N) was calculated. Peptides with summed S/N lower than 100 across all channels or isolation specificity lower than 0.5 were discarded. The high confidence peptides were then used to quantify protein abundance by summing up S/N values for all peptides assigned to the same protein, and only proteins in the linear quantification range of the instrument were included in the analysis. The normalization for protein quantification was then performed by adjusting protein loadings of total sum of S/N values to that of every TMT channel.

Statistical Overrepresentation Test

Statistical overrepresentation analysis/test of proteins pulled down with Biotin-(1S,3R)-RSL3 was performed on the portion of the hit list that met all the following criteria: 1) >1 peptide identified by TMT-MS, 2) p-value < 0.050, 3) fold enrichment > 2. This list of genes was then input into PANTHER database (v18.0) and analyzed for protein class overrepresentation. As selenoproteins are not annotated as a protein class in this current version of PANTHER, we calculated the probability of observing a selenoprotein in a random set of genes from the human genome as 25/20592 (utilizing the reference list size of PANTHER v18.0). This probability value was scaled to our input list and a Fisher's exact t-test was performed for statistical significance.

C11-BODIPY lipid ROS measurement (flow cytommetry)

Indicated cells were seeded in 12-well plates and allowed to adhere overnight at 37 °C prior to beginning the indicated treatment or targeted gene knockdown induced by doxycycline. Cells were harvested using PBS-EDTA (5 mM), buffer, washed once with HBSS, suspended in HBSS containing 5 μM C11-BODIPY (Thermo Fisher), and incubated at 37 °C for 30 min. Cells were pelleted, washed, and resuspended in HBSS. Fluorescence intensity was measured on the FITC channel using the Beckman Coulter MoFlo Astrios. A minimum of 20,000 cells were analyzed per condition. Data were analyzed using FlowJo software (Tree Star). Values are expressed as MFI.

Synergy Calculations

Synergy was calculated through disproof of the null hypothesis that treatment with two biologically active compounds would produce a result in line with the Bliss Model of Independence as previously described[24].

ICP-MS

Whole blood from indicated mice were obtained via submandibular vein puncture or from the orbital sinus. Whole blood was collected in untreated sterile 1.5 mL Eppendorf tubes and allowed to coagulate for 1-2 hrs at RT. Coagulated samples were spun at 13,000xg for 15 min and serum was collected. Collected serum was further clarified with a second spin at 13,000xg for 15min. 10 μL of clarified serum was treated with 2 mL/g total wet weight nitric acid (20 μL) (Trace metal grade; Fisher) for 24 hr, and then digested with 1 mL/g total wet weight hydrogen peroxide (10 μL) (Trace metal grade; Fisher) for 24 h at room temperature. The samples were preserved at 4 °C until quantification of metals. Ultrapure water (VWR Chemicals ARISTAR®ULTRA) was used for final sample dilution to 3 mL. Samples were then analyzed using inductively coupled plasma mass spectrometry (ICP-MS) (Perkin Elmer) utilizing Bismuth as an internal standard.

T-cell isolation

T-cells were isolated from total blood according to previously established protocols[25]. Whole blood from indicated mice was obtained via submandibular vein puncture or from the orbital sinus and collected into sterile 1.5 mL Eppendorf tubes. 100 μL of whole blood from each mouse was then immediately transferred into a new sterile 1.5 mL Eppendorf tube containing 50 μL 0.5 M EDTA, pH 8. Tubes were kept on ice until all samples were collected for processing. If

any signs of coagulation were observed, samples were discarded and re-collected. The entire blood sample for each mouse (150 µL) was transferred into a 15 mL Eppendorf tube containing 5 mL of room temperature (RT) ACK red blood cell lysis buffer (Gibco), briefly vortexed, and incubated at RT for 3 minutes. After incubation the samples were placed back on ice and the reaction was stopped by addition of 8 mL of ice cold T-cell culture medium (RPMI supplemented to final concentrations of 10% FBS, 2 mM L-Glutamine, 0.1 mM 2-mercaptoethanol (BME), and 1% Penicillin-Streptomycin). Samples were centrifuged at 400xg for 4 min at 4 °C, supernatant was discarded by vacuum, and cell pellets were resuspended in 200 µL T-cell culture medium. Samples were kept on ice for a short time until ready for processing by Flow Cytommetry with antibodies as indicated in the figure legend.

Auranofin Diet

Auranofin Diet was made from powdered laboratory rodent diet (LabDiet) mixed with appropriate quantities of drug in a KitchenAid mixer designated for laboratory use. Diet dosing was calculating assuming an average mouse weight of 25 g and chow consumption of 4 g/day as previously published[26]. Water was added to a hydration level of 60% (600 mL H_2O per kg of diet) and thoroughly mixed. Small quantities of food-grade coloring (McCormick) were added to differentiate doses of diet. Following mixing, diet was extruded into pellets and dehydrated for 72 hrs with a food dehydrater at 41 °C (Nesco). Mice were not provided an alternate food source when undergoing treatment and weight was routinely monitored.

Xenograft studies

MC38 (C57Bl/6J) or CT26 (Balb/c) cell lines were maintained for 2 weeks at less than 70% confluency prior to injection into fully immune-competent C57Bl/6J or Balb/c mice. Prior to injection, cells were trypsinized, thoroughly washed, and resuspended in sterile saline to a final injection volume of 100 µL. Wildtype mice of both sexes were anesthetized via inhaled isoflurane (induction dose 3-4%, maintenance dose 1-2%) and inoculated with 2 million MC38 or 0.4 million CT26 cells. Cells were implanted into lower flanks and treatment began at day 4 (CT26) or day 10 (MC38) once palpable tumors were identified. Tumor size was measured with digital calipers utilizing the formula $V=0.5*L*W^2$.

Ethical endpoints for xenograft studies were determined in accordance with Association for Assessment and Accreditation of Laboratory Animal Care International guidelines and approved by the University Committee on the Use and Care of Animals at the University of Michigan.

Ethical endpoints for this study were determined to be any of the following: 30 days post implantation, tumor size exceeding 2 cm in any direction, hemorrhage of the tumor, or indications of tumor induced pain and decreased mobility. Once endpoint was determined for any of the groups, all mice in study were euthanized by CO_2 inhalation and tumors were excised. Tumor volume and weight were measured, and tissues were prepared for histology, IHC, or flow cytometry as indicated. A licensed veterinarian was available for consult at all points during the study.

AOM/DSS induction of colitis-associated colorectal cancer

C57BL/6J mice were utilized to model colitis-associated colon cancer. In this model, mice are administered a single injection of azoxymethane (AOM), followed by 3x cycles of dextran sodium sulfate (DSS) administered in drinking water. Cycles last for 7 days on DSS with a 14-day recovery. Ethical endpoints were established at weight loss > 20% from cycle start, or signs of pain and distress that did not rapidly resolve in the recovery period. No mice in these studies were lost to ethical endpoint concerns.

At 6 weeks of age mice were weighed and injected intraperitoneally with 10 mg/kg of AOM. Three days following AOM injection mice began their first cycle of 2% (w/v) DSS water administered via dripper bottle. No alternative water source was provided. Mice were weighed 3x/week while on DSS water. A DSS cycle was considered successful upon the observation of moderate weight loss not exceeding ethical guidelines and/or observations of loose and/or bloody stool. Following a DSS cycle, mice began a 14 day recovery period before the next cycle of DSS treatment. A successful recovery period was determined by weight gain from the last reading of the DSS cycle and resolution of any loose and/or bloody stool. For the second and third DSS cycles, the DSS concentration was increased to 2.5% (w/v). Treatment with Auranofin chow began immediately following the conclusion of the 3rd administration of DSS water and continued for 30 days. A licensed veterinarian was available for consult at all points during the study. Following euthanasia, the abdominal cavity was opened and the entirety of the large intestine (cecum to rectum) was isolated. The proximal colon was then separated from the cecum and the cecum was discarded. The colon was flushed with PBS, split longitudinally, and the mucosal layer was scraped. The flattened colon was fixed by application of 10% formalin and tumors were manually counted and sized by a study-blinded participant. The colon was then swiss-rolled, pinned, and transferred to an inclusion cassette. Inclusion cassettes were submerged in 10% formalin overnight and transferred to 70% ethanol prior to paraffin

embedding for histology. Histological analysis was performed via a study-blinded independent pathologist.

Glutathione Peroxidase Activity Assay

Total cellular glutathione peroxidase activity was measured using Glutathione Peroxidase Assay kit (fluorometric) (Abcam). Lysates were prepared in SDS-free lysis buffer and analyzed according to the provided protocol. Readings were obtained via microplate reader and normalized to an untreated control. Technical triplicate readings were obtained and averaged for each biological replicate.

Thioredoxin Reductase Activity Assay

Thioredoxin Reductase (TxnRD) Activity assay was based on the plate reader procedure as outlined by Cunnif *et al.*, Anal. Biochem, 2013[27] and established by Arnèr *et al.*, Methods in Enzymology, 1999[28]. Briefly, the TxnRD activity assay is based on consumption of the diselenide amino acid selenocystine in cell lysate, measured by NADPH consumption via absorbance at 340 nm on a spectrophotometric plate reader (Cytation 5, BioTek). TxnRD is the only cellular enzyme capable of reducing selenocystine, consuming NADPH in the process. A master-mix of 2 mM NADPH and 1 mM selenocystine was prepared fresh for each assay. NADPH (Sigma Aldrich) solution was prepared in 100 mM Tris, pH 8; fresh solution was used whenever possible and solution was used within 1 week if frozen at -20 °C, with reduced initial absorbance observed when utilizing thawed NADPH. As selenocystine does not readily dissolve in aqueous buffer, selenocystine (Cayman Chemical Company) was first dissolved in 1N NaOH (650 µL for a 50 mg vial), to which ½ volume of 1N HCl was added to neutralize the solution. The master stock was then diluted to 45 mM in ddH2O and stored at -20 °C. Cells were plated and treated as indicated, washed in PBS, and lysed in RIPA buffer. The insoluble fraction was removed via centrifugation (13,000xg, 10 min, 4 °C) and protein abundance was quantified by BCA Protein Assay (Thermo Scientific). 50 µg of protein was utilized per well in a total volume of 60 µL, to which 40 µL of NADPH/Selenocystine master-mix was added. Immediately following addition of the master-mix (within 2 min), kinetic reading of absorbance values was initiated, with reads taken every 60 s for 30 min.

CRISPR Co-Essentiality Network Generation

CRISPR gene effect scores from the DepMap 22Q2 release were first corrected using Cholesky whitening as previously described[29]. A matrix of p-values corresponding to gene-wise Pearson

correlations was calculated from the whitened data, then converted to FDR values using the p.adjust() function in R. A network was then constructed from all partners within 2 edge distances from a given gene of interest, using an FDR cutoff of 0.05 to define edges/partnership. Network graphs were generated from pairwise gene lists using the tidygraph and ggraph packages in R, with the layout argument in ggraph set to “graphopt”

<u>AGB 364/366 synthesis</u>

Scheme 1. Synthesis of Cpd24 and Biotinylated Analog[a]

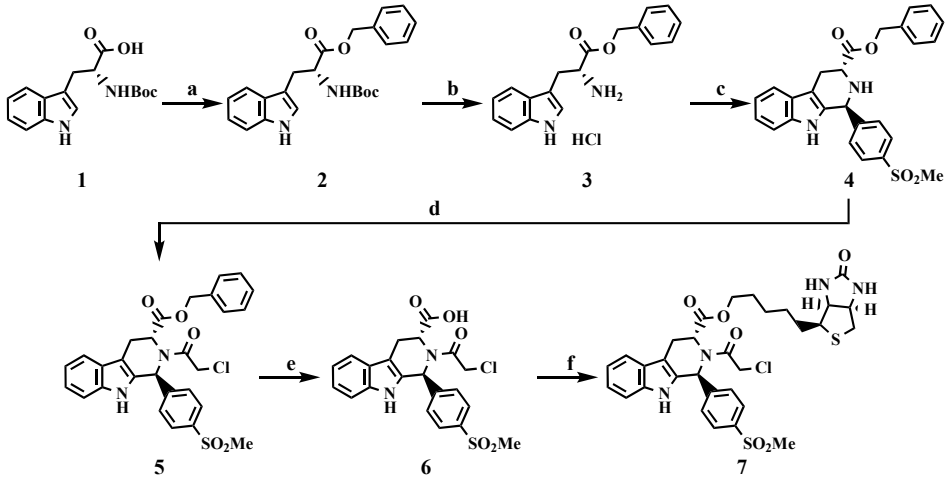

[a]Reagents and conditions: (a) BnOH, EDC, DMAP, THF, rt, overnight; (b) 4 N HCl in 1,4-dioxane, rt, overnight, 92% over 2 steps; (c) 4-(methylsulfonyl)benzaldehyde, IPA, reflux, 87%; (d) $ClCH_2C(O)Cl$, TEA, CH_3CN, reflux, 87%; (e) H_2, Pd/C, EtOH, rt, overnight, 72%; (f) *D*-biotinol, EDC, DMAP, THF, rt, overnight, 4%.

Scheme 2. Synthesis of RSL3 and Biotinylated Analog[b]

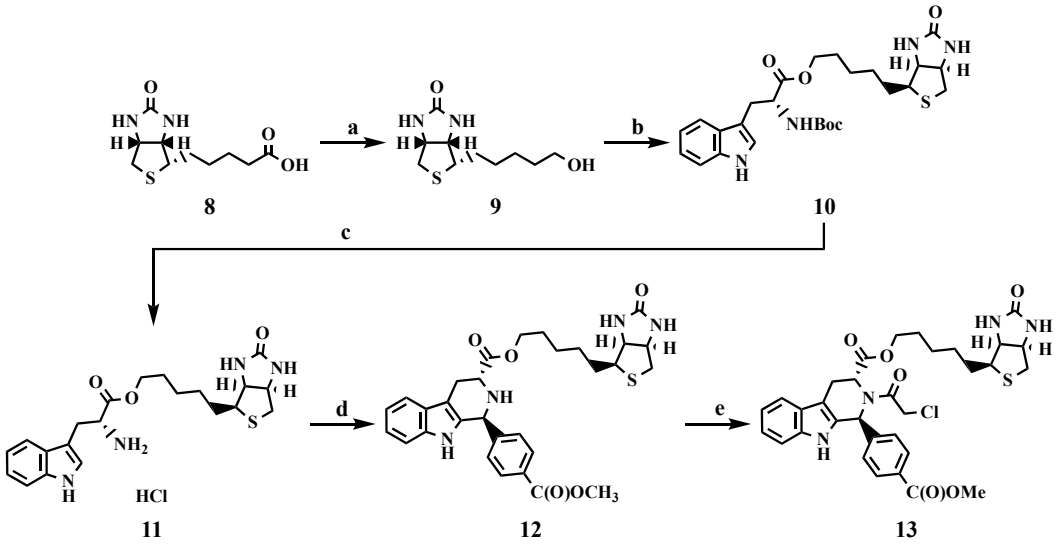

[b]Reagents and conditions: (a) $LiAlH_4$, THF, reflux, overnight, 45%; (b) (*tert*-butoxycarbonyl)-*D*-tryptophan, EDC, DMAP, THF, rt, overnight, 74%; (c) 4 N HCl in 1,4-dioxane, rt, overnight, 91%; (d) methyl 4-formylbenzoate, IPA, reflux, 15%; (e) $ClCH_2C(O)Cl$, TEA, CH_3CN, reflux, 19%.

Statistics.

Data are represented as mean ± standard deviation. unless otherwise indicated. Data are from a minimum of 3 independent experiments measured in triplicate unless otherwise stated in the figure legend. For statistical analyses, unpaired *t*-tests were conducted to assess the differences between 2 groups. One-way or 2-way ANOVA was used for multiple treatment conditions followed by Tukey's post hoc test. A strict p-value cutoff of < 0.050 was utilized for determination of significance in all experiments. All statistical tests were carried out using Prism 10 software (GraphPad).

Study approval.

All animal studies were carried out in accordance with Institute of Laboratory Animal Resources guidelines and approved by the University Committee on the Use and Care of Animals at the University of Michigan (IACUC protocol number: PRO00011805)

Results

The potency of (S)-RSL3 is due to GPx4 independent effects in CRC cell lines.

Ferroptotic cell death is largely attributed to overwhelming of the ability of GPx4 to detoxify lipid peroxides. Several mechanisms have been demonstrated to induce GPx4 dependent ferroptosis, such as inhibition of System Xc- to limit glutathione synthesis[30], or knockdown of LRP8 to inhibit selenium import for GPx4 translation[31]. However, the most commonly utilized mechanism of ferropototic induction is treatment with the small molecule RSL3 (Figure 1A). RSL3 has two stereoisomers, (1S,3R)-RSL3 and (1R,3R)-RSL3, which we will refer to as (S) and (R)-RSL3, respectively (Figure 1B). Previously, the (S) and (R) stereoisomers of RSL3 have been characterized as differentially targeting GPx4[18], with the ability of (S)-RSL3 to inhibit GPx4 thought to directly correlate with its increased potency through induction of ferroptosis. Utilizing 72 hr live cell imaging growth assays we confirmed that (S)-RSL3 is markedly more potent than (R)-RSL3 in the HT1080 fibrosarcoma cell line that is frequently utilized in ferroptosis research[32]. The EC_{50} values of 13 nM for (S)-RSL3 and 900 nM for (R)-RSL3 (Figure 1C, S1A) are consistent with previously reported cell death and viability measurements[13]. However, both (S)-RSL3 and (R)-RSL3 exhibited nearly equipotent sensitivity in CRC cell lines DLD1, HCT116, RKO, and SW480, with EC_{50} values at ~1 μM. Notably, DLD1 cells displayed a 2-fold increased sensitivity to (R)-RSL3, despite the inability of (R)-RSL3 to inhibit GPx4 (Figure 1D).

In contrast to other forms of regulated cell death, ferroptosis lacks specific cellular markers and is instead assessed through the ability to rescue cell death with lipid-ROS scavenging agents such as Liproxstatin-1 (Lip-1)[12]. In our growth assays, we aimed to delineate the "ferroptotic window" induced by (S) and (R)-RSL3 through Lip-1 co-treatment. Despite broad cell line sensitivity to (S)-RSL3, the ferroptotic window varied significantly between cell lines and often did not result in a complete rescue of (S)-RSL3 treatment (Figure 1D, S1B). In agreement with previous data, (R)-RSL3 induced decreases in cell growth were unable to be rescued by Lip-1 at any dose in our cell line panel (Figure S1C). The equipotent nature of these two compounds led us to hypothesize that while GPx4 inhibition likely drives ferroptosis, the potency of (S)-RSL3 in CRC cell lines may be driven by a GPx4-independent activity of this compound.

RSL3 sensitivity does not predict GPx4 essentiality in CRC cell lines

To investigate if (S)-RSL3 functions independently of its ability to inhibit GPx4 in CRC, we generated stable cell lines with doxycycline inducible GPx4 shRNAs (GPx4 i-KD). Two RNA guides for GPx4, sh2, and sh3, were found to decrease GPx4 levels by >95% at 72 hrs post

doxycycline treatment (Figure 2A). GPx4 was confirmed to be essential for cell growth in the CRC cell lines SW480, RKO, and HCT116, however the DLD1 line was insensitive to GPx4 i-KD despite sensitivity to (S)-RSL3 (Figure 2B). Furthermore, near complete GPx4 i-KD in DLD1 cells resulted in a 10-fold increase in sensitivity to (S)-RSL3 (Figure 2C, S2A). These data argue strongly for and support the hypothesis that the potency of (S)-RSL3 in CRC cells can be due to GPx4-independent effects. We additionally tested a next generation GPx4 inhibitor, the ML210[33] derivative JKE1674[34]. JKE1674 is markedly less potent than (S)-RSL3 across CRC cell lines and is inactive up to 20 μM in the DLD1 cell line (Figure 2D). JKE1674 exhibits significantly lower potency in CRC lines as compared to (S)-RSL3, and the decreases in growth induced by JKE1674 are rescued by Lip-1 as demonstrated in the RKO cell line (Figure 2E).

These data raise numerous questions. DLD1 cells are sensitive to ferroptosis, indicating that there is a pre-existing intrinsic imbalance of intracellular peroxide regulation. However, if DLD1 cells are insensitive to inhibition or loss of GPx4, there must exist a secondary method of peroxide regulation in these cells. While the majority of ferroptosis research focuses on glutathione peroxidases, cells indeed possess a secondary method of peroxide detoxification, the thioredoxin peroxidases, known as peroxiredoxins (PRDXs)[35]. PRDXs serve as sacrificial peroxide detoxifying enzymes, donating electrons to break down H_2O_2 and forming an internal disulfide bridge. PRDXs must then be recycled by thioredoxins and the NADPH-dependent selenoprotein thioredoxin reductase (TxnRD) before they are active once more[36] (Figure 2F). TxnRD activity can serve as a proxy for activity of the thioredoxin peroxidase redox system[28] and recent work has demonstrated RSL3 can directly target TxnRD1[37]. We observe that the DLD1 cell line has ~2-3-fold higher TxnRD activity than other CRC cell lines (Figure 2G, S2B). These data suggest that the DLD1 cell line more heavily utilizes the thioredoxin peroxidase system for regulation of intracellular H_2O_2, perhaps explaining the observed insensitivity to GPx4 i-KD and JKE1674.

Choloracetamide based ferroptosis inducers non-selectively inhibit the selenoproteome

While we can replicate recent studies demonstrating that (S)-RSL3 inhibits TxnRD1 activity[37] (Figure S3A) – potentially explaining why (S)-RSL3 is still active in our DLD1 cells – we wished to further investigate the spectrum of (S)-RSL3 targets to identify new therapeutic targets in CRC that may have been masked behind the ability of (S)-RSL3 to inhibit GPx4. To revisit the characterization of (S)-RSL3 we synthesized a biotinylated derivative, utilizing the same attachment site at the 3 position as the original publication[13] (Figure 3A). The synthesis yielded

a small quantity of biotinylated (R)-RSL3 which we used to validate that the biotin group did not alter the potency of these compounds (Figure 3B). Following optimization of pull-down protocol, including 1 μM selenium supplementation to increase trace selenoprotein expression (Figure S3B), streptavidin-based pull-downs of (S)-RSL3 vs biotin-(S)-RSL3 were performed on biological triplicates. The use of Tandem Mass Tag (TMT) labeling combined with the use of next-generation mass spectrometers has offered unparalleled sensitivity, revealing that while (S)-RSL3 does inhibit GPx4, it is also a broadly non-specific inhibitor (Figure 3C). However, we suspect that many of these targets may not be pharmacologically relevant, as the reactive chloroacetamide moiety utilized in RSL3 is known to be highly reactive and broadly non-specific[38]. We thus further explored the targets of chloroacetamide based ferroptosis inducers with the RSL3 derivative Cpd24[39], observing near identical results (Figure S3C). Thus, we performed protein class statistical overrepresentation analysis through the PANTHER classification system to narrow down our dataset. Statistical overrepresentation analysis reveals two heavily enriched protein classes as targets of (S)-RSL3, peroxidases and selenoproteins (Figure 3D-E).

Glutathione peroxidases 1 and 4 (GPx1/4) and TxnRD1 were found in our datasets, thus validating the assay and previous results[18,37]. We also pulled down nearly the entirety of the thioredoxin peroxidase system, identifying the peroxiredoxins PRDX1-4 as novel targets of (S)-RSL3. These data suggest that the effects of (S)-RSL3 on intracellular ROS extend beyond lipid peroxide detoxification and instead may be due to broad dysregulation to detoxify intracellular peroxides. Interestingly, we identified a large number of selenoproteins as targets of RSL3. While PANTHER does not classify selenoproteins as a protein class, manual investigation of our dataset revealed that out of the top 20 most enriched targets in our RSL3 pulldown, 10 were selenoproteins or binding partners of selenoproteins. In sum we identified 11 selenoproteins (Sel F, Sel H, Sel K, Sel M, Sel N, Sel S, GPx1, GPx4, TxnRD1, SEPHS2, MSRB2) in our datasets, adding 9 new selenoproteins to the list of RSL3 targets. While selenoproteins are heavily understudied, they are known to regulate many redox functions within the cell, including ROS detoxification and oxidative protein folding[40]. Thus, our data suggests that in addition to its ability to inhibit GPx4, the potency of (S)-RSL3 may also be due to its lack of specificity and broad ability to inhibit the selenoproteome.

Auranofin, a selenoproteome inhibitor, induces oxidative stress and ferroptosis in CRC

With the discovery that RSL3 likely functions through pan-inhibition of the selenoproteome, we next sought to investigate the therapeutic potential of Auranofin. Auranofin is an orally bioavailable gold salt that is FDA approved for the treatment of rheumatoid arthritis[41,42]. Auranofin is a compound *S*-glycosyl gold salt, comprised of a 2,3,4,6-tetra-O-acetyl-1-thio-beta-D-glucopyranose sugar with the sulfur atom coordinated to a (triethylphosphoranylidene)gold functional group. Once Auranofin enters the cell, the (triethylphosphoranylidene)gold separates from the carrying sugar and reacts with selenocysteine residues to form an Au-Se inhibitory adduct[43,44]. While Auranofin is typically considered an inhibitor of Thioredoxin Reductase 1 (TxnRD1), preventing oxidative protein folding and peroxiredoxin recycling to potently induce oxidative stress[45,46], recent data demonstrate that the true mechanism of Auranofin is the non-specific formation of Au-Se adducts, revealing Auranofin to be a broad selenoprotein inhibitor[47–49] - similar to our recharacterization of RSL3 (Figure 4A). To investigate the therapeutic potential of Auranofin in CRC we performed dose response curves across our CRC cell line panel. We observed a potent decrease in growth across all tested CRC cell lines and several cell lines displayed statistically significant rescue by Lip-1 (Figure 4B). These data suggest that Auranofin is a novel inducer of ferroptosis (in a dose and cell line specific manner) through its ability to broadly target the selenoproteome in CRC.

We next sought to further characterize the non-ferroptotic mechanisms of Auranofin, as Auranofin is a potent inducer of apoptosis in other cell lines[50]. While all tested concentrations of Auranofin could be completely rescued by the general antioxidant N-Acetyl Cysteine (NAC), we observed some cell line specific rescue that was statistically significant, but not complete, with the apoptosis inhibitor Z-Vad-FMK[51,52] or the necroptosis inhibitor Nec-1[53] (Figure 4C). These findings support the characterization of Auranofin as an inducer of oxidative stress. However, the exact cell death mechanism induced by oxidative stress appears to be both dose and cell line dependent, with some doses of treatment capable of partial rescue with multiple different cell death inhibitors. However, when Auranofin levels are increased to the μM range, growth can no longer be rescued with Lip-1, Z-Vad, or Nec-1, indicating that high doses of Auranofin induce a non-specific form of oxidative cell death, consistent with what was observed with (S)-RSL3.

We observe that following GPx4 i-KD, the potency of Auranofin was slightly increased; however, we also drastically shift the primary mechanism of Auranofin treatment to ferroptosis as determined by Lip-1 rescue (Figure 4F). Altogether our data support a model where (S)-RSL3 activity is driven through its ability to function as a pan-inhibitor of the selenoproteome:

simultaneously targeting thioredoxin peroxidases to induce oxidative stress, and GPx4 to shift the mechanism of oxidative cell death to ferroptosis.

Investigating the selenoproteome as a therapeutic target in CRC through AlkBH8 i-KD

To confirm that general inhibition of the selenoproteome is an efficacious target for therapeutic intervention in CRC, a genetic approach to modulate the selenoproteome is required. To guide our approach, co-essentiality analysis revealed that Gpx4 and TxnRD1 are co-essential across CRC cell lines, along with the bulk of the tRNA-sec biosynthetic pathway (Figure S5A-B). From these analyses, we identified the tRNA-methyltransferase AlkBH8 as a potential novel therapeutic target in CRC, as high AlkBH8 expression correlates with decreased overall survival in CRC patients (Figure 5A-B). AlkBH8 has been extensively reported to regulate the selenoproteome via methylation of tRNA-selenocysteine, with AlkBH8 knockdown and knockout models demonstrating a decreased ability to translate selenoproteins[54–61]. We observed that AlkBH8 expression is significantly increased in tumor tissue as compared to normal controls (Figure 5C), and that patients with early-onset CRC have increased expression of AlkBH8 as compared to all other age groups (Figure 5D). As AlkBH8 possesses two druggable domains[57,62] and could be a target for future development of targeted therapies for early onset-CRC, we sought to experimentally investigate the role of AlkBH8 in altering the selenoproteome and cell growth in CRCs.

Two guides for AlkBH8 i-KD (sh3/4) were found to induce knockdown of AlkBH8 by 60% (sh3) and 80% (sh4) respectively (Figure 6A). In agreement with prior literature, we observed that AlkBH8 i-KD led to an inability to translate selenoproteins as observed through a time-dependent decrease of GPx4 (Figure 6B). Furthermore, we observed a 40% reduction in TxnRD activity 72 hrs post AlkBH8 KD (Figure 6C), supporting the ability of AlkBH8 i-KD to genetically replicate the mechanism of (S)-RSL3. To further investigate the therapeutic potential of AlkBH8 in CRC the i-KD cell lines were maintained in doxycycline media to assess growth and colony formation. A significant decrease in growth and colony formation was observed across all tested CRC cell lines with no effects observed in NCM460, a normal human colon mucosal epithelial cell line, (Figure 6E-F) supporting our hypothesis that AlkBH8 is a novel therapeutic target in CRC with a potential therapeutic window. Taken together, our data suggest that modulation of the selenoproteome is a viable therapeutic strategy in CRC and may be the underlying mechanism through which (S)-RSL3 is capable of broad activity across CRC cell lines, independent of individual cell line sensitivity to inhibition or knockdown of GPx4.

Targeting the selenoproteome reduces CRC growth *in-vivo*

We next sought to validate our *in-vitro* findings in an *in-vivo* setting. For these studies, we utilized the CT26 cell line – a mouse derived colorectal adenocarcinoma cell line – suitable for syngeneic xenografts in fully immunocompetent Balb/c mice. After confirmation that CT26 cells were responsive to Auranofin treatment and displayed a ferroptotic window (Figure S7A-B), $0.4x10^6$ cells were implanted to each flank of Balb/c mice and treatment with Auranofin (10 mg/kg, IP, daily) began at 4 days after implantation once tumors were palpable. At the study endpoint we observed that IP treated mice displayed a consistent 30% reduction in final tumor mass (Figure 7A), with histological staining demonstrating signs of intra-tumoral necrosis (Figure 7B). However, we were unable to rescue this phenotype with simultaneous administration of Lip-1 (10 mg/kg, IP, daily) indicating that this mechanism of *in-vivo* activity was independent of Auranofin's ability to induce ferroptosis. Dose optimization performed on non-tumor bearing mice demonstrated that Auranofin administration via chow was much better tolerated than IP administration, perhaps through limitation of handling stress on the animals (Figure S7C). Furthermore, plasma levels of Auranofin can be measured through analysis of serum gold concentration by inductively coupled plasma mass spectrometry (ICP-MS) revealing that diet administration of Auranofin allows for an *in-vivo* dose response, demonstrating dose-dependent increases in plasma gold, and identical endpoint plasma gold concentrations between 10 mg/kg administration independent of dosing route (Figure S7D). Furthermore, our ICP-MS data demonstrate that mice administered 10 mg/kg Auranofin display plasma gold levels equivalent to patients receiving 6 mg/day Auranofin[63], estimated at plasma concentrations reaching ~1 μM[64]. While there are scores of differences between mouse and human physiology, our data suggest that the dose of Auranofin necessary to cause tumor cell death *in-vivo* is clinically achievable. We next repeated our CT26 xenograft study with our in-house formulated dose response chow and observed similar effectiveness in tumor growth reduction across all tested doses of Auranofin chow (Figure S7E). Flow cytometry analysis of Auranofin treated tumors confirmed differential *in-vivo* mechanisms, with only low dose Auranofin chow capable of inducing intra-tumoral lipid-ROS (Figure S7F), supporting the potential of Auranofin as an orally bioavailable therapeutic option in CRC that can induce *in-vivo* ferroptosis.

However, CRC has a unique microenvironment in the colon that is not recapitulated in a flank xenograft model. Therefore, we aimed to use the AOM/DSS model of chemical carcinogen-induced colorectal cancer to study the effects of Auranofin on a diverse population of cells within

the native microenvironment. We chose to use 2.5 mg/kg Auranofin chow for this study as it was the lowest effective dose in flank xenograft studies. Furthermore, as 2.5 mg/kg Auranofin chow was observed to induce lipid-ROS in our flank tumors, this dose allowed us to study the effects of *in-vivo* induction of ferroptosis on CRC initiation. Mice were administered a single injection of AOM intraperitoneally followed by 3x 7-day cycles of DSS water (2%, 2.5%, 2.5%) with a two-week recovery period between cycles. Immediately after the last cycle of DSS, mice were administered Auranofin chow *ad-libitum* and remained on Auranofin chow for the remainder of the study. Mice were euthanized on d30 and colons were extracted, flushed, and split longitudinally to visualize the lumen. Microscopic visual analysis confirmed presence of colorectal tumors in both groups (Figure 7C). While the total number of tumors per mouse trended lower in the treated mice, statistical analysis was non-significant between the groups. However, there was a significant reduction in tumor size and total tumor burden in the Auranofin treated group (Figure 7D). Histological analysis further confirmed the presence of multiple colorectal adenocarcinomas in both groups (Figure 7E-F), however the tumors of the untreated control group were significantly more advanced than those in the treated group. While the treated group still displayed multiple regions of neoplasia, low dose Auranofin treatment lessened the extent to which these regions developed into aggressive lesions – further demonstrating the potential of Auranofin as a targeted therapeutic agent for CRC.

Discussion

Ferroptosis represents a targetable mechanism with high potential for cancer therapeutics. Yet, ferroptosis research has predominantly relied on investigations using small molecules, which can be confounded by unknown off-target effects. In this study, we observe that the effectiveness of (S)-RSL3 in CRC may stem from its GPx4-independent functions. Despite a broad sensitivity to (S)-RSL3, not all CRC cell lines respond to GPx4 inhibition. Consequently, our findings shed light on the reduced potency observed with the synthesis of next-generation GPx4 inhibitors such as JKE1674, where heightened target engagement may paradoxically diminish activity. While RSL3 remains a potent ferroptosis inducer, our data adds to its characterization and demonstrates that it is not solely a GPx4 inhibitor, revealing numerous additional targets such as thioredoxin peroxidases and selenoproteins.

This recharacterization of RSL3 unveils a binary system of redox regulation in CRC cells, wherein the Txn and GPx systems prevent the toxic byproducts of ROS addiction. While a majority of the investigations into ferroptosis in CRC focus on the activity of GPx4, our study suggests that the TxnRD and peroxiredoxin systems might equally contribute by directly detoxifying H_2O_2 prior to hydroxyl radical formation. Auranofin is a small molecule gold-based selenoprotein inhibitor that is FDA-approved for the treatment of rheumatoid arthritis but has been broadly studied for its anti-tumor properties. However, Auranofin is primarily characterized as an inducer of apoptosis, whereas in CRC we observe that Auranofin can induce ferroptosis and non-specific oxidative cell death. Auranofin treatment in established tumors leads to reduced tumor growth with observations of intra-tumoral necrosis suggesting that Auranofin can induce tumor cell death *in-vivo* at clinically achievable doses. Furthermore, our studies of low dose Auranofin suggest that Auranofin can limit CRC initiation and progression. As an inexpensive and orally bioavailable compound, the therapeutic potential of Auranofin opens the doors for new studies of *in-vivo* induction of oxidative stress and ferroptosis.

Furthermore, we show that RSL3 is a non-specific inhibitor of the selenoproteome and reveal a novel therapeutic target in CRC: the tRNA methyltransferase AlkBH8. Our data demonstrate the essential role of AlkBH8 for the growth of multiple CRC cell lines, with negligible effects observed on the normal colon cell line NCM460 upon AlkBH8 knockdown (KD). Supporting this data, whole-body knockout mice lacking AlkBH8 exhibit no discernible defects, and individuals with homozygous AlkBH8 mutations show a non-lethal phenotype, indicating tolerability to

complete loss of AlkBH8 activity. Importantly, AlkBH8 features two druggable domains— an AlkB Fe(II)/α-ketoglutarate-dependent dioxygenase domain and a methyltransferase domain. Although full-length recombinant AlkBH8 and its substrates remain uncharacterized, we anticipate that their development will facilitate small molecule inhibitor discovery, potentially yielding targeted therapies for CRC.

Our exploration into the selenoproteome underscores the potential of this underexplored protein class. To produce a mere 25 enzymes, nature has evolved an intricate network of protein machinery capable of incorporating the highly reactive and toxic trace metal selenium. While the biology of selenoproteins remains enigmatic, the chemistry has been well characterized. Selenium is orders of magnitude more efficient in reacting with and detoxifying ROS, coinciding with the majority of selenoproteins being involved in the regulation of oxidative stress. However, only a fraction of the selenoproteome has been investigated to decipher their roles in human biology, and even less for their involvement in cancer development and progression. While our approaches employing AlkBH8 KDs or gold and chloroacetamide warheads to target the selenoproteome yield non-selective selenoprotein inhibition, we posit that deeper investigations into selenoproteins may not only advance our understanding of redox biology but also unveil novel therapeutic targets.

Acknowledgements

The authors would like to acknowledge the members of the Shah and Koutmos laboratories for project feedback and manuscript editing. This work was funded by NIH grants R01CA148828, R01CA245546, and R01DK095201 (Y.M.S.), UMCCC Core grant P30CA046592 (Y.M.S.), CA286898 and GM117141 (M.K.), NIH/NIGMS grant R01GM132129 (J.A.P.) and NIH grant R01DK124384 to JDM. JDM holds patents for methods for modulating ferritinophagy. JDM reports research support from Novartis and Casma Therapeutics and has consulted for Third Rock Ventures and Skyhawk Therapeutics, all unrelated to the work

Author Contributions

SLD, MK, and YMS initiated the project, performed or directed all experiments, and wrote the manuscript. SD assisted with the majority of experiments. SS was heavily involved in training and assistance for in-vivo studies. LZ, MOD, NKD, CC, HNB, YZ, NJR, EM, JH, ZS, and IT assisted with in-vitro, bioinformatic, and/or in-vivo experiments. MS, JP, and JM performed Mass Spectrometry studies. AB and NN synthesized RSL3 derivatives.

Figure 1

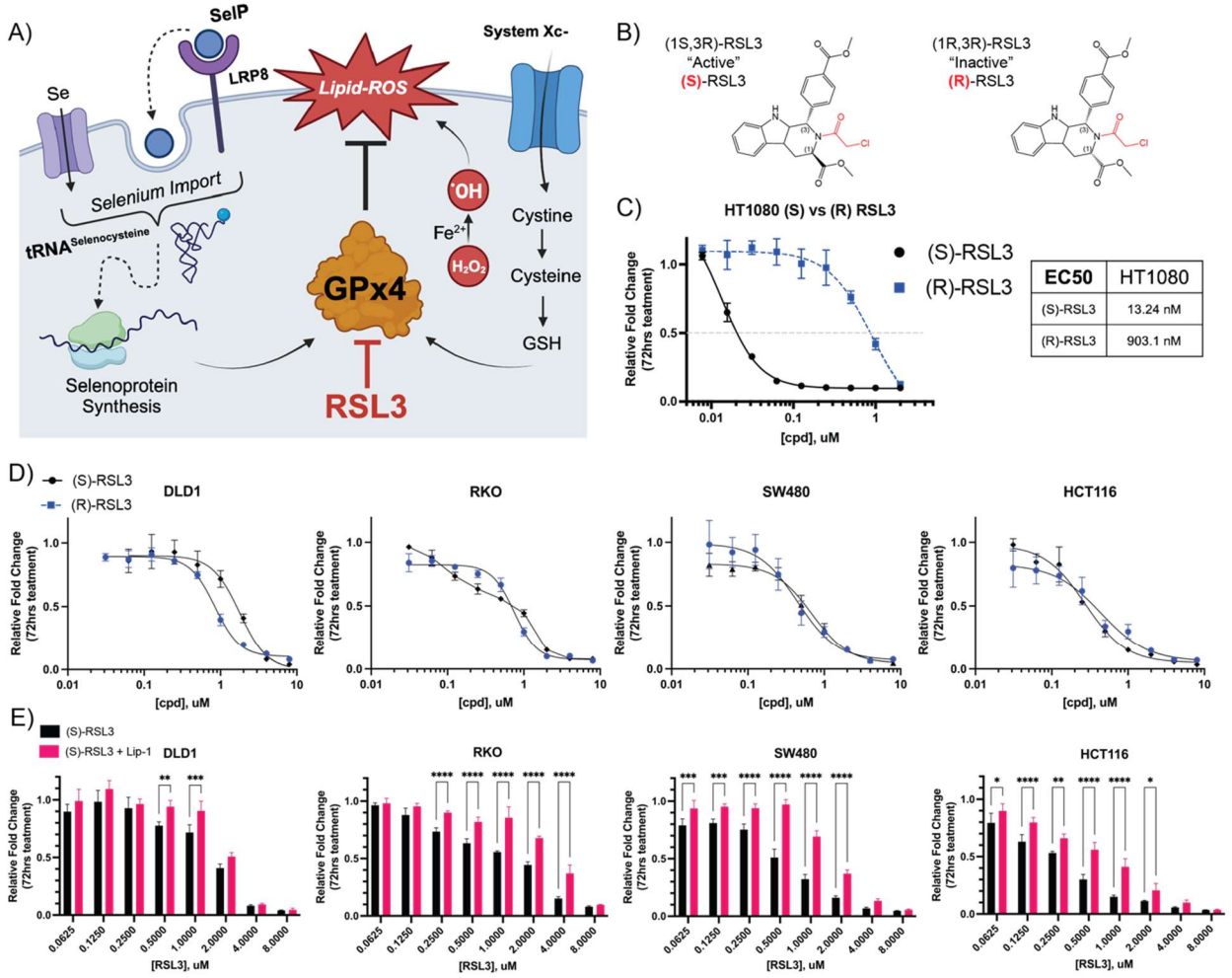

Figure 1: Defining the ferroptotic window of S-RSL3 in CRC cell lines.
A) Schematic of current understanding of ferroptosis, where the ability of GPx4 to detoxify ROS induced lipid peroxides (Lipid-ROS) is regulated by GSH synthesis driven by System Xc- import of Cystine and selenium availability in part by LRP8 which is then incorporated into the GPx4 polypeptide by tRNA-selenocysteine. GPx4 can be inhibited by RSL3. B) Structures of (1S,3R)-RSL3 and (1R,3R)-RSL3. C/D) Cell growth normalized to untreated control at 72 hr following (S) or (R) RSL3 treatment in HT1080 and CRC cell lines. E) Calculation of the "ferroptotic window" of (S)-RSL3 across a panel of CRC cell lines, where a ferroptosis driven response is calculated by a statistically significant rescue of growth by co-treatment with liproxstatin-1 (Lip-1) (1 μM). *: $p < 0.05$, **: $p < 0.01$, ***: $p < 0.001$, ****: $p < 0.0001$

Figure S1

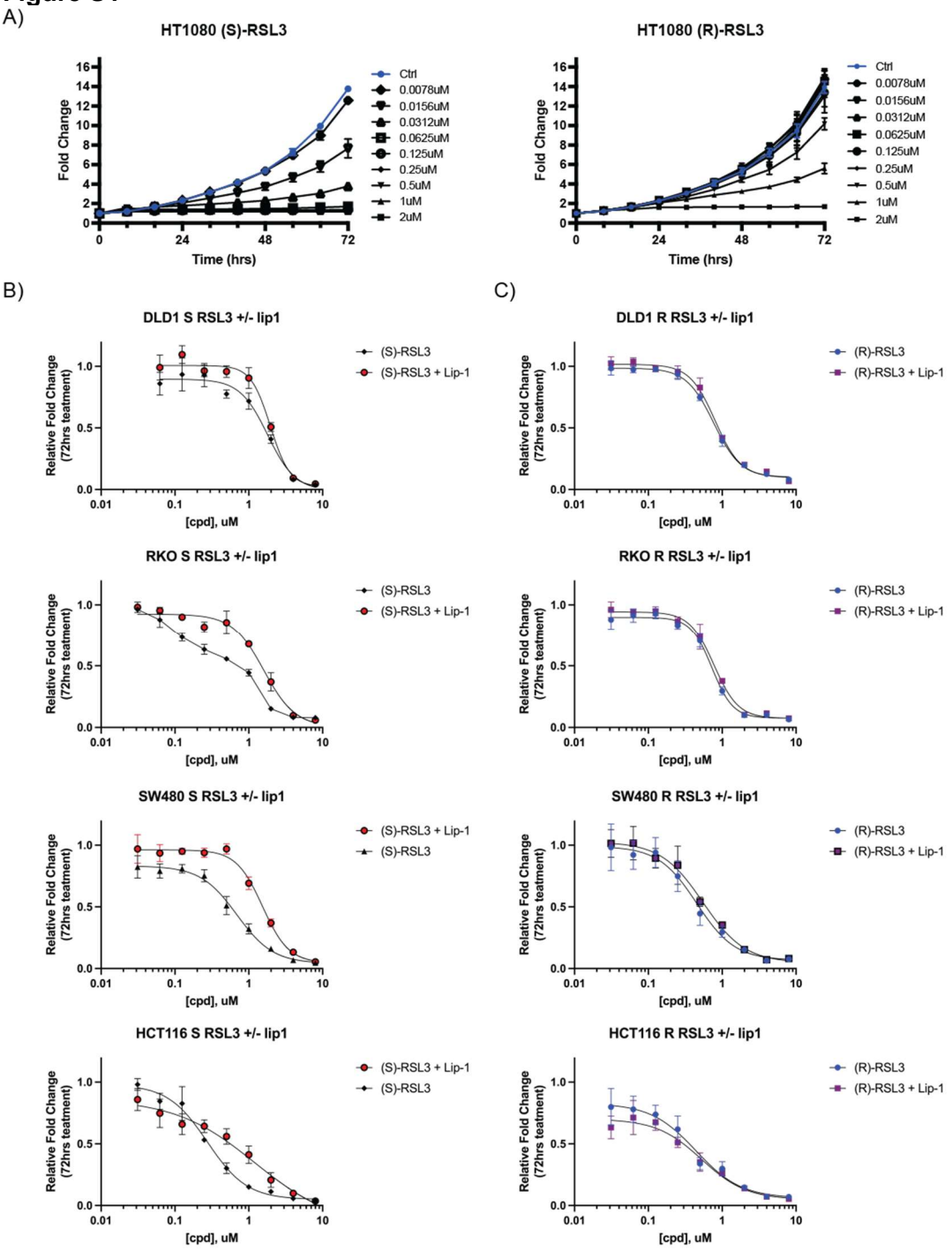

Figure S1

A) Original growth assay data utilized for EC50 value calculations of HT1080 dose response to (S) and (R) RSL3. Cell growth is normalized to read at t0 with reads taken by Cytation 5 with BioSpa every 8 hrs. At endpoint, values are normalized to the average growth of untreated control wells. B) Dose response curves of CRC cell lines treated with (S)-RSL3 +/- Lip-1 (1 μM). C) Dose response curves of CRC cell lines treated with (R)-RSL3 +/- Lip-1 (1 μM)

Figure 2

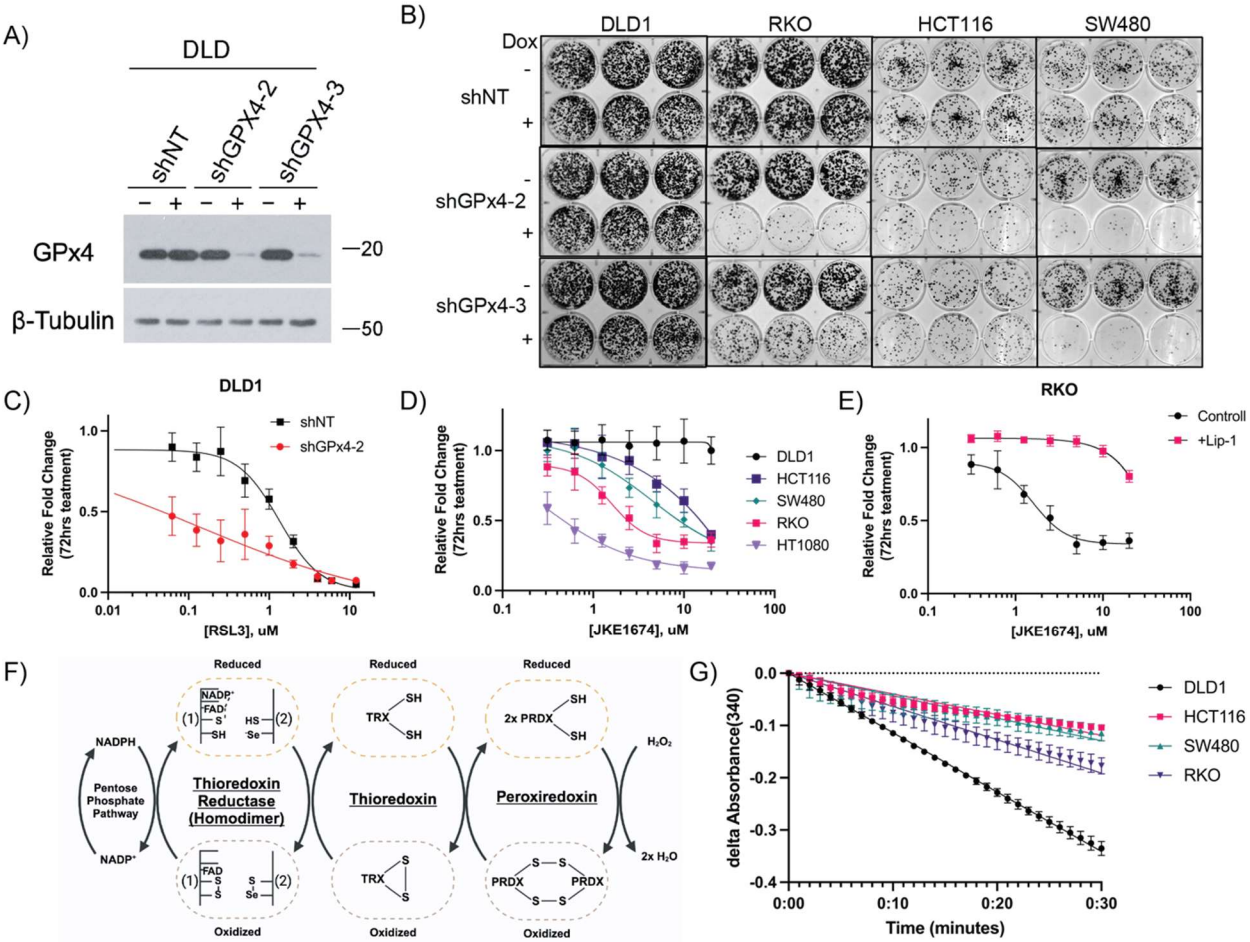

Figure 2: Elucidating the role of GPx4 in CRC cell lines.
A) Western blot of stable DLD1 doxycycline inducible shRNA cell lines (shNT, shGPx4-2, shGPx4-3), +/- doxycycline treatment (250 ng/mL) assessed at 72 hrs, β-Tubulin was used as a loading control. B) Colony formation assays of indicated stable shGPx4 or shNT cell lines treated +/- doxycycline (250ng/mL) assessed at 2 weeks. C) 72 hr live cell growth assay dose response of RSL3 in DLD1 shNT vs shGPx4-2 cell line, both pre-treated with doxycycline (250 ng/mL) for 72 hrs prior to addition of (S)-RSL3. D) 72 hr live cell growth JKE1674 dose response of CRC cell lines and HT1080. E) 72 hr live cell growth assay JKE1674 dose response of the RKO CRC cell line, either untreated or pre-treated with 1 μM Lip-1. F) Schematic of the mechanism of the Thioredoxin Reductase-Peroxiredoxin system, where NADPH from the Pentose Phosphate Pathway is utilized in the selenoprotein Thioredoxin Reductase to recycle oxidized 2-Cys Peroxiredoxins after the redox mediated detoxification of hydrogen peroxide, forming a Peroxiredoxin dimer. G) Thioredoxin Reductase Kinetic Activity Assay measuring NADPH consumption through reduction of NADPH absorbance at 340 nm upon addition of NADPH and Selenocystine to cell lysates

Figure S2

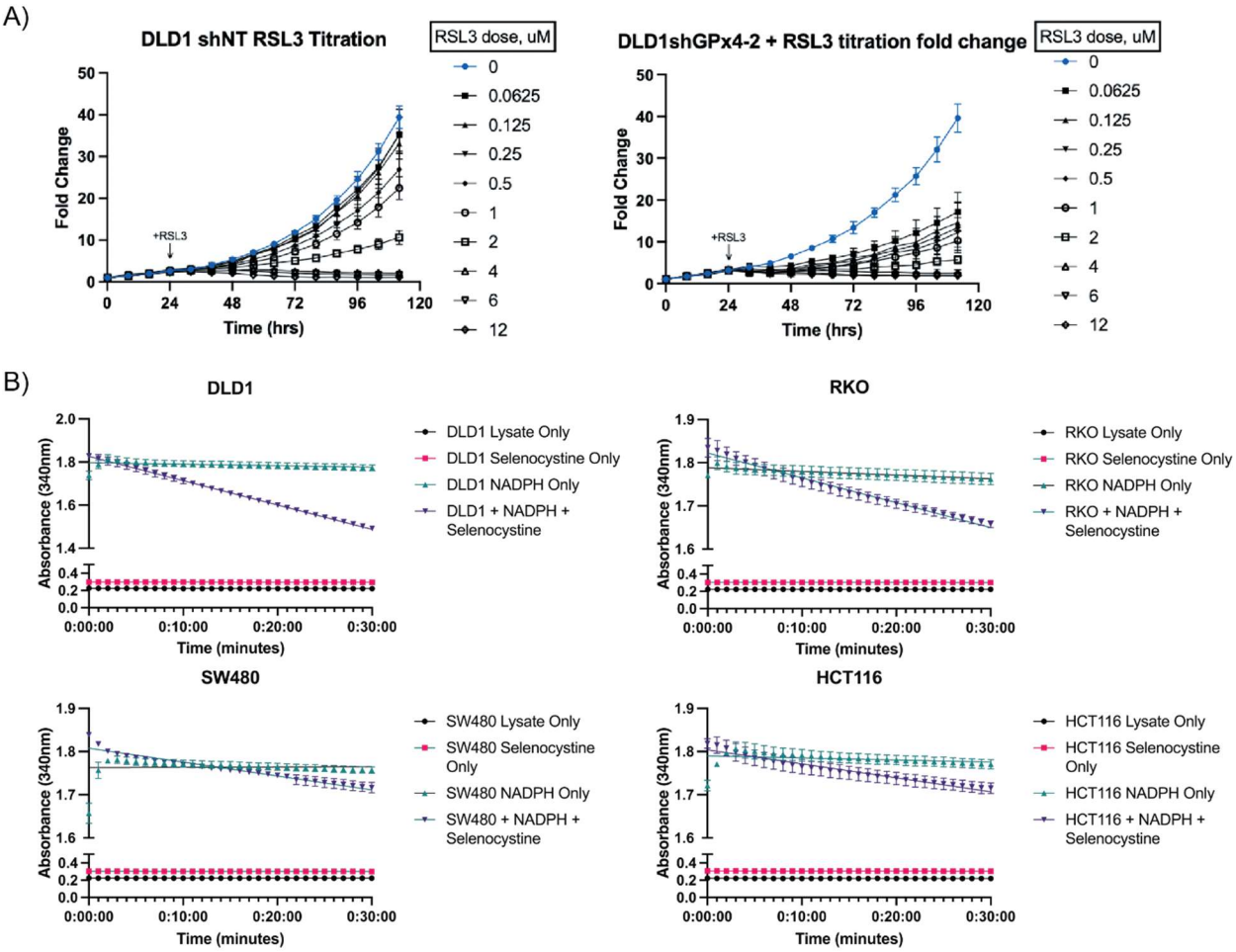

Figure S2
A) Live Cell Proliferation assay of DLD1 shNT vs shGPx4 cell line (+dox) treated with indicated doses of (S)-RSL3. Cells were pre-treated with doxycycline for 48 hrs prior to first imaging and imaged for 24 hrs prior to treatment with (S)-RSL3. B) Internal controls utilized for the thioredoxin reductase kinetic activity assay. Absorbance at 340 nm was measured every 60 s for 30 min on a Cytation 5 plate reader. Wells contained either lysate only, lysate + selenocystine, lysate + NADPH, or lysate + selenocystine/NADPH master mix as indicated. 3 technical replicates were averaged for each point and plotted as mean +/- SD

Figure 3

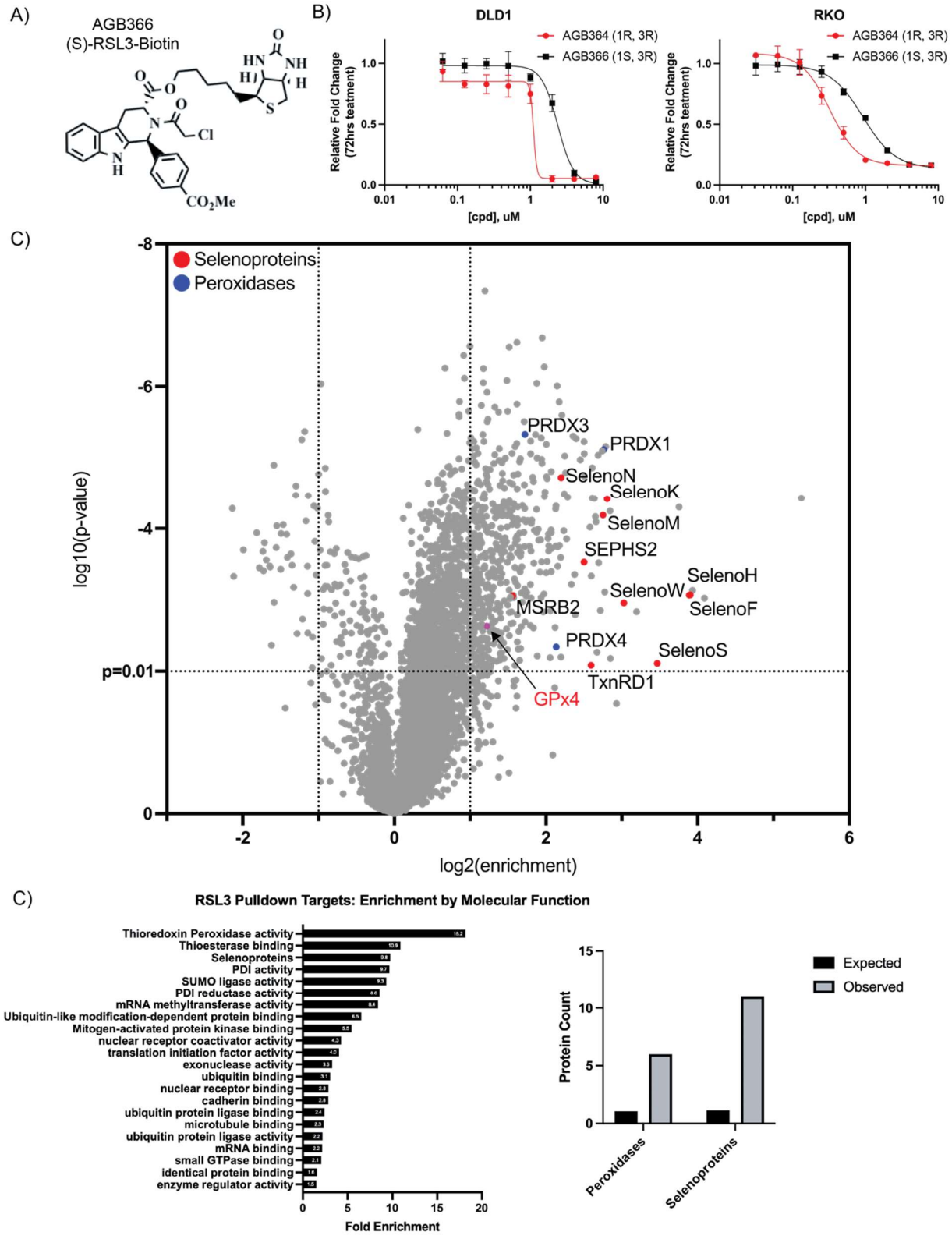
A)
AGB366
(S)-RSL3-Biotin
B)
DLD1
AGB364 (1R, 3R)
AGB366 (1S, 3R)
Relative Fold Change (72hrs teatment)
[cpd], uM
RKO
AGB364 (1R, 3R)
AGB366 (1S, 3R)
Relative Fold Change (72hrs teatment)
[cpd], uM
C)
Selenoproteins
Peroxidases
PRDX3
PRDX1
SelenoN
SelenoK
SelenoM
SEPHS2
SelenoH
SelenoW
SelenoF
MSRB2
PRDX4
SelenoS
TxnRD1
GPx4
p=0.01
log10(p-value)
log2(enrichment)
C)
RSL3 Pulldown Targets: Enrichment by Molecular Function
Thioredoxin Peroxidase activity
Thioesterase binding
Selenoproteins
PDI activity
SUMO ligase activity
PDI reductase activity
mRNA methyltransferase activity
Ubiquitin-like modification-dependent protein binding
Mitogen-activated protein kinase binding
nuclear receptor coactivator activity
translation initiation factor activity
exonuclease activity
ubiquitin binding
nuclear receptor binding
cadherin binding
ubiquitin protein ligase binding
microtubule binding
ubiquitin protein ligase activity
mRNA binding
small GTPase binding
identical protein binding
enzyme regulator activity
Fold Enrichment
Protein Count
Expected
Observed
Peroxidases
Selenoproteins

Figure 3: Affinity Pulldown-Mass Spec Redefines RSL3 as a Selenoprotein Inhibitor
A) Structures of biotinylated RSL3 derivative used for these studies, AGB366. B) 72 hr live cell growth assays of AGB364/366 in DLD1 and RKO cells normalized to untreated control. C) Affinity-Pulldown Mass Spec analysis of AGB366 ((S)-RSL3-Biotin) from RKO lysate with targets of interest identified. D) RSL3 Pulldown targets protein class enrichment (PANTHER) and number of peroxidases and selenoproteins observed in the AGB366 pulldown dataset vs. expected by random chance.

Figure S3

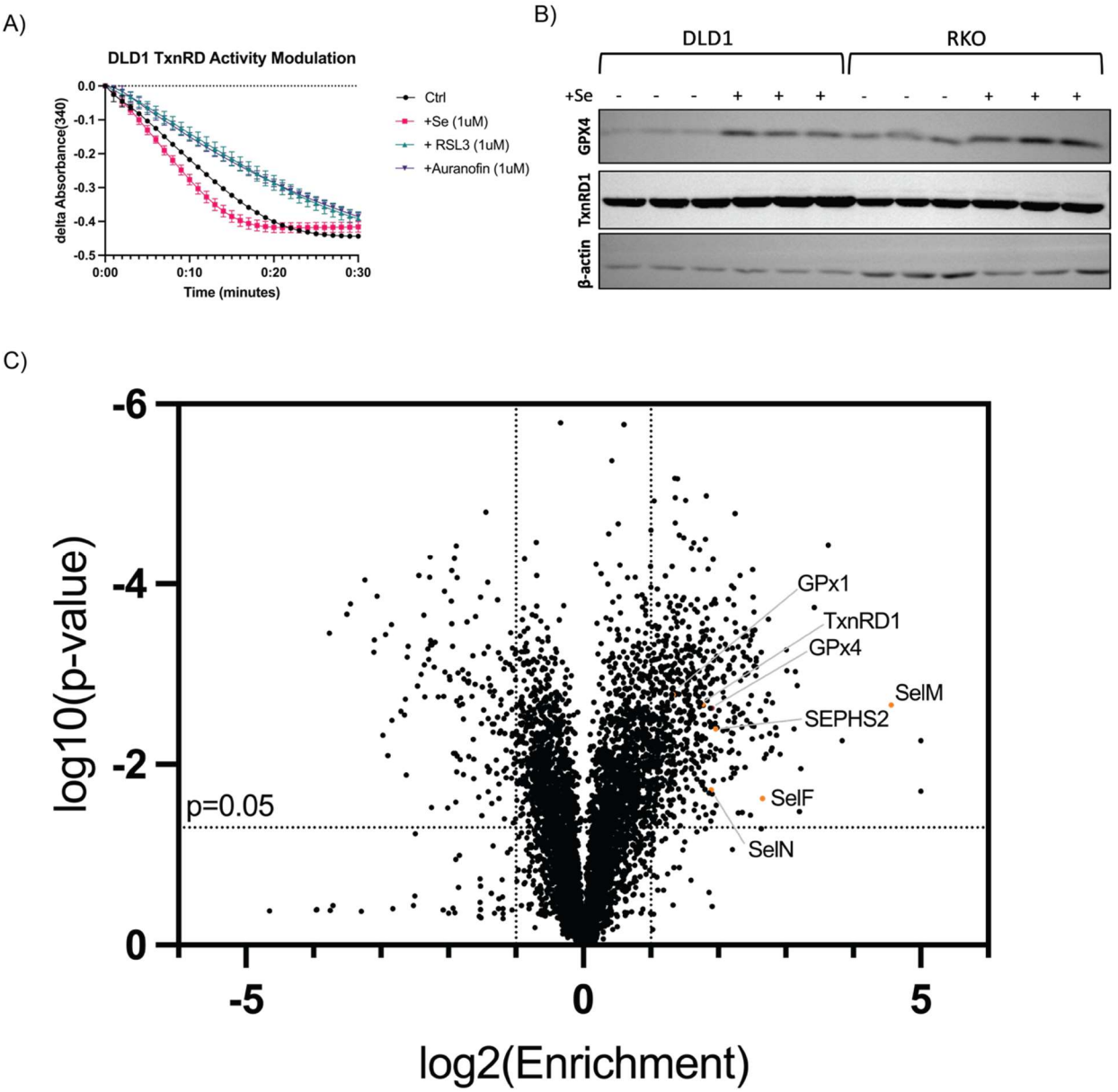

Figure S3

A) Modulation of TxnRD1 activity in DLD1 cells through 24 hr treatment with 1μM sodium selenite, 1 μM (S)-RSL3, or 1 μM Auranofin. Flattening of the curve at later time points is due to complete consumption of NADPH in the reaction. B) Western Blot of GPx4 and TxnRD1 expression levels in DLD1 and RKO cell lines using biological triplicates +/- 24 hr supplementation with 1 μM sodium selenite. C) AP-MS results of Cpd24-Biotin using RKO cell lysate compared to mock AP-MS pulldown using the non-biotinylated compound

Figure 4

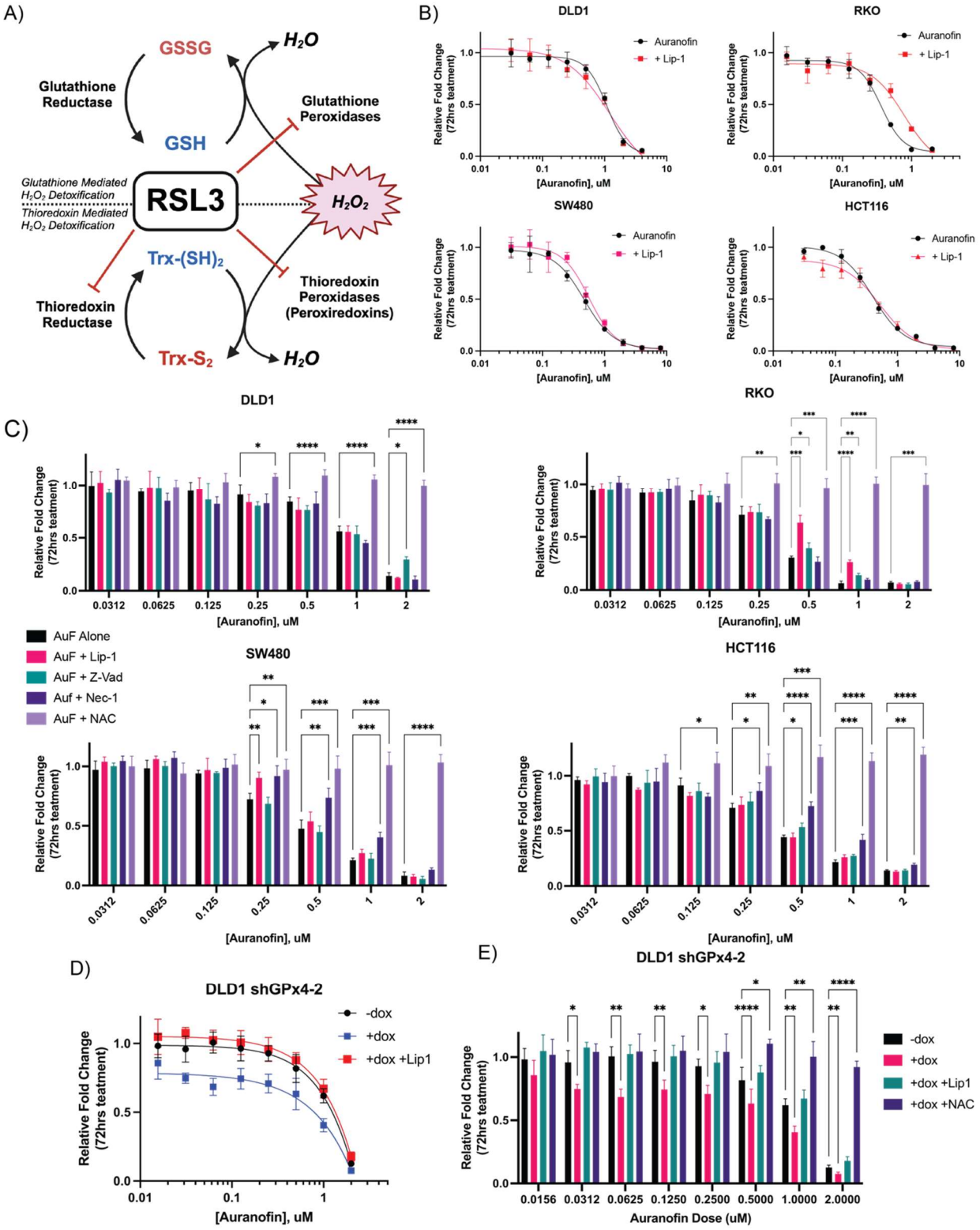
A)
GSSG
H_2O
Glutathione Reductase
Glutathione Peroxidases
GSH
Glutathione Mediated H_2O_2 Detoxification
Thioredoxin Mediated H_2O_2 Detoxification
RSL3
H_2O_2
Trx-(SH)$_2$
Thioredoxin Peroxidases (Peroxiredoxins)
Thioredoxin Reductase
Trx-S$_2$
H_2O
B)
DLD1
RKO
SW480
HCT116
Auranofin
+ Lip-1
Relative Fold Change (72hrs teatment)
[Auranofin], uM
C)
DLD1
RKO
SW480
HCT116
AuF Alone
AuF + Lip-1
AuF + Z-Vad
Auf + Nec-1
AuF + NAC
Relative Fold Change (72hrs teatment)
[Auranofin], uM
D)
DLD1 shGPx4-2
-dox
+dox
+dox +Lip1
Relative Fold Change (72hrs teatment)
[Auranofin], uM
E)
DLD1 shGPx4-2
-dox
+dox
+dox +Lip1
+dox +NAC
Relative Fold Change (72hrs teatment)
Auranofin Dose (uM)

Figure 4: Auranofin Can Induce Ferroptosis in CRC

A) Schematic of the new proposed mechanism of RSL3 activity where RSL3 as a pan-inhibitor of the selenoproteome can inhibit both glutathione and thioredoxin reductases as well as peroxiredoxins. B) 72 hr live cell growth assays of CRC cell lines treated with Auranofin +/- Liproxstatin-1 (1 μM) co-treatment normalized to untreated control. C) Full rescue panel of Auranofin across CRC cell lines from 72hr live cell growth assay with indicated co-treatments: Lip-1 (1 μM), Z-vad-FMK (10 μM), NAC (10 mM), Nec1 (10 μM). D) 72 hr live cell growth assay of the DLD1 shGPx4-2 cell line treated as indicated (untreated control, 250 ng/mL doxycycline, 1 μM Lip-1) and normalized to untreated control. Cells were pretreated with doxycycline or vehicle (ddH_2O) for 72 hrs prior to first imaging and treatment with Auranofin

*: $p < 0.05$, **: $p < 0.01$, ***: $p < 0.001$, ****: $p < 0.0001$

Figure 5

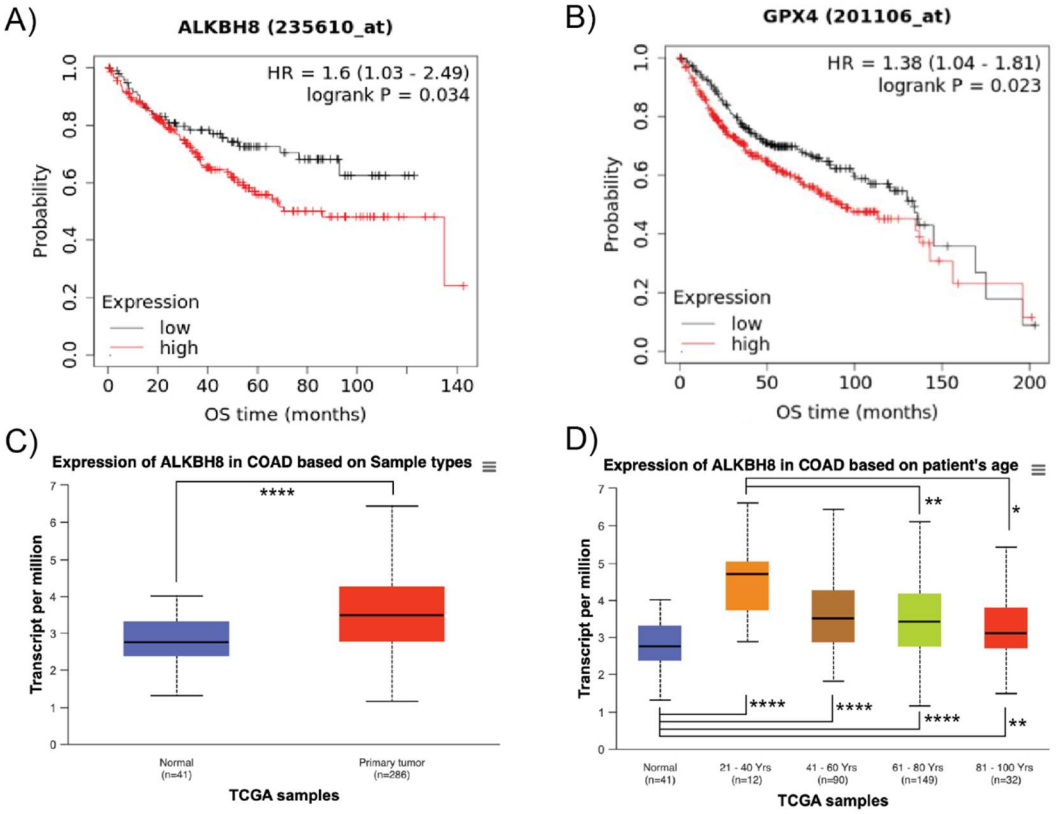

Figure 5: AlkBH8 is a potential therapeutic target in CRC.

A) Kaplan-Meier overall survival analysis of CRC patients based on RNA-seq measured expression levels of AlkBH8. B) Kaplan-Meier overall survival analysis of CRC patients based on RNA-seq measured expression levels of GPx4. C) TCGA analysis of normal vs. tumor samples analyzed for AlkBH8 expression. D) TCGA analysis of AlkBH8 expression in CRC tumor samples by age.

*: $p < 0.05$, **: $p < 0.01$, ***: $p < 0.001$, ****: $p < 0.0001$

Figure S5

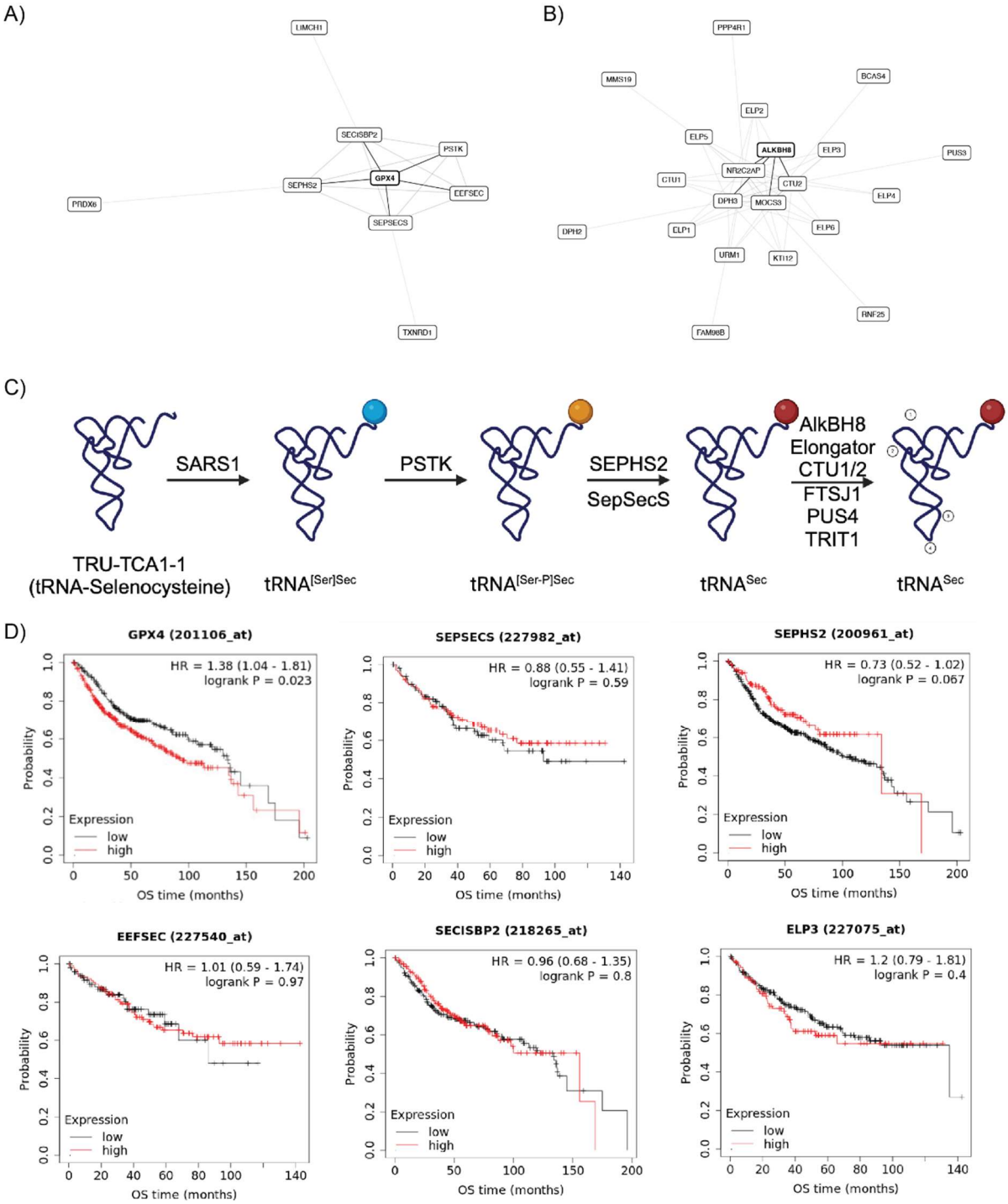

Figure S5

A) CRISPR co-essentiality network map of GPx4 co-dependencies. B) CRISPR co-essentiality network map of AlkBH8 co-dependencies in CRC cell lines. C) Biosynthetic pathway of tRNA-Selenocysteine. D) Km plots of select genes in the tRNA-sec pathway – not all genes had significant patient numbers to perform a high-powered analysis

Figure 6

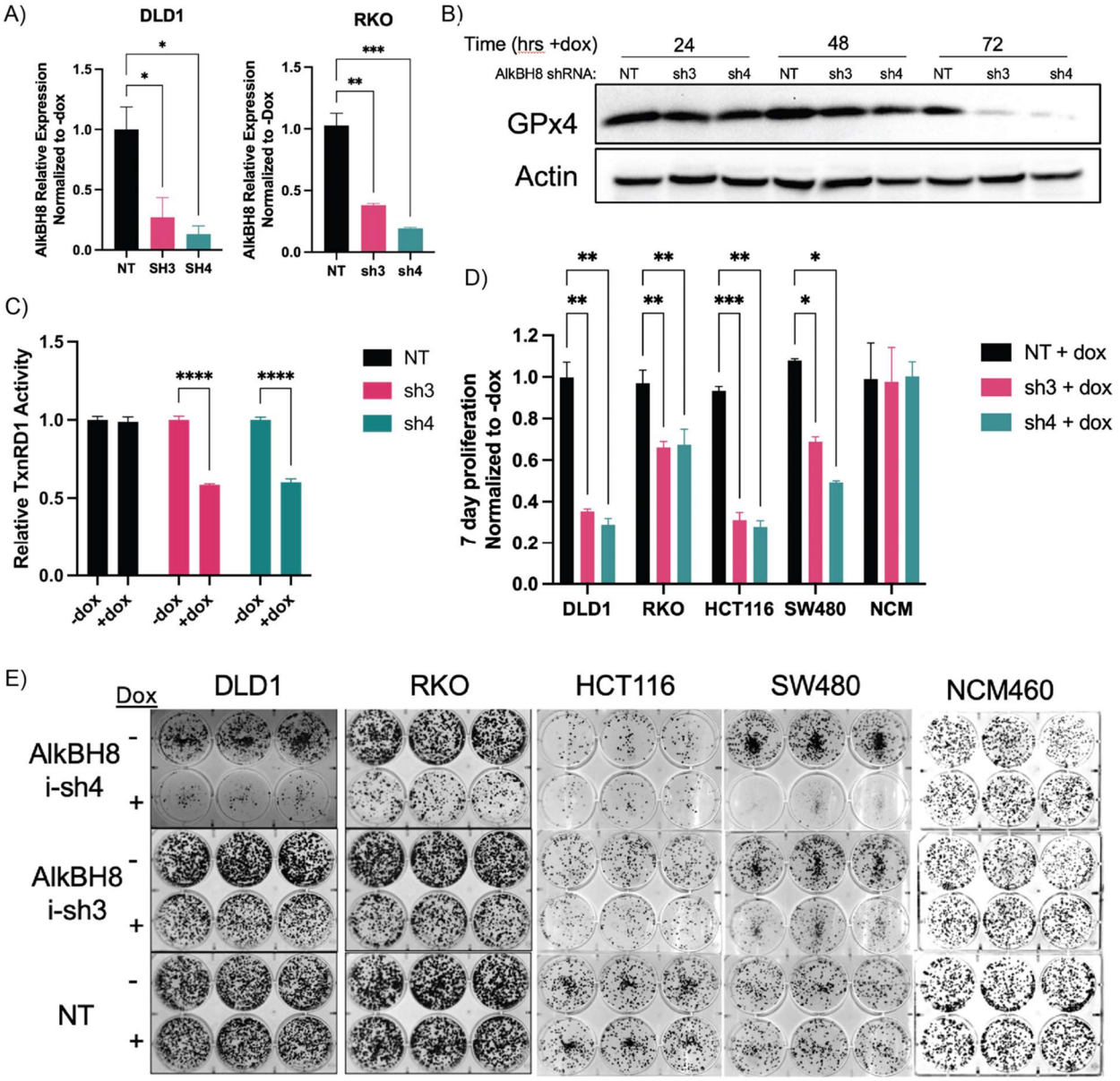

Figure 6: AlkBH8 regulates the selenoproteome and is essential for CRC growth *in-vitro.*

A) qPCR analysis of AlkBH8 expression levels (normalized to untreated controls) following 72 hr treatment with doxycycline (250 ng/mL). B) Western Blot analysis of GPx4 levels in the DLD1 shAlkBH8 cell lines at indicated time points following doxycycline treatment. C) TxnRD activity assay in DLD1 shAlkBH8 lysates +/- doxycycline treatment (72 hrs) as indicated. D) 7-day proliferation assay results of shAlkBH8 cell lines following doxycycline treatment, normalized per cell line to untreated control wells. E) Colony formation assays of CRC shAlkBH8 cell lines grown for 2 weeks +/- doxycycline as indicated

*: $p < 0.05$, **: $p < 0.01$, ***: $p < 0.001$, ****: $p < 0.0001$

Figure 7

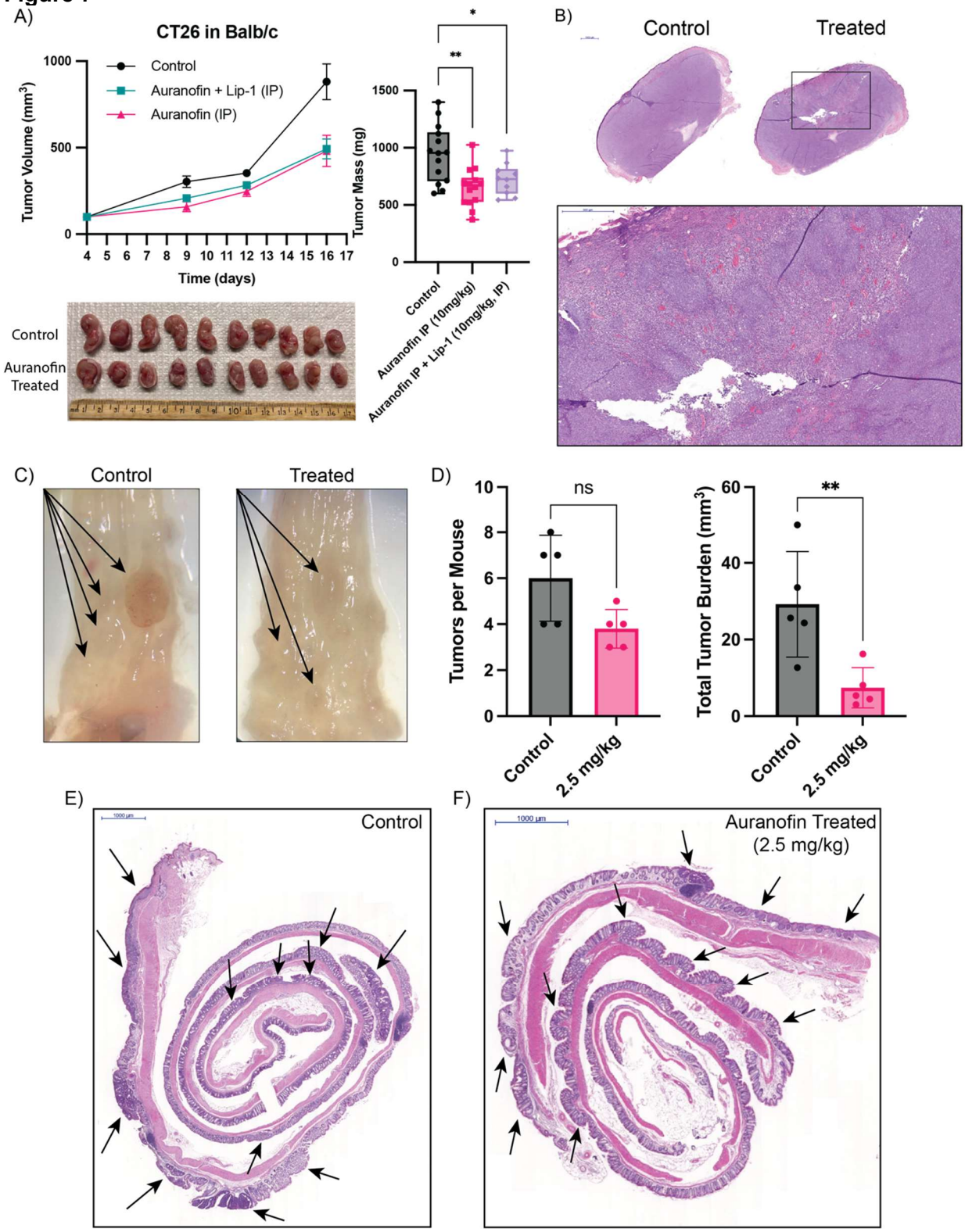
A)
CT26 in Balb/c
Control
Auranofin + Lip-1 (IP)
Auranofin (IP)
Tumor Volume (mm³)
Time (days)
Tumor Mass (mg)
Control
Auranofin IP (10mg/kg)
Auranofin IP + Lip-1 (10mg/kg, IP)
Control
Auranofin Treated
B)
Control
Treated
C)
Control
Treated
D)
ns
Tumors per Mouse
Total Tumor Burden (mm³)
Control
2.5 mg/kg
E)
Control
F)
Auranofin Treated
(2.5 mg/kg)

Figure 7: Auranofin is an effective treatment in *in-vivo* models of CRC.
A) Flank xenograft implant studies of CT26 cells in Balb/c mice treated as indicated displaying caliper estimated tumor volume measurements, final measured tumor mass, and tumor images. B) H&E staining of Auranofin treated vs control tumor with higher magnification of a region of interest in the treated tumor. C) Representative microscopy pictures of control and treated colons (Auranofin 2.5 mg/kg) following AOM/DSS induction of colorectal cancer with visually detectable tumors marked by arrows. D) Quantification of tumor number and total tumor burden (mm^3) per mouse colon following AOM/DSS induction. E-F) H&E staining of swiss-rolled colons from C. Notable regions of dysplasia are marked by arrows.
*: $p < 0.05$, **: $p < 0.01$, ***: $p < 0.001$, ****: $p < 0.0001$

Figure S7

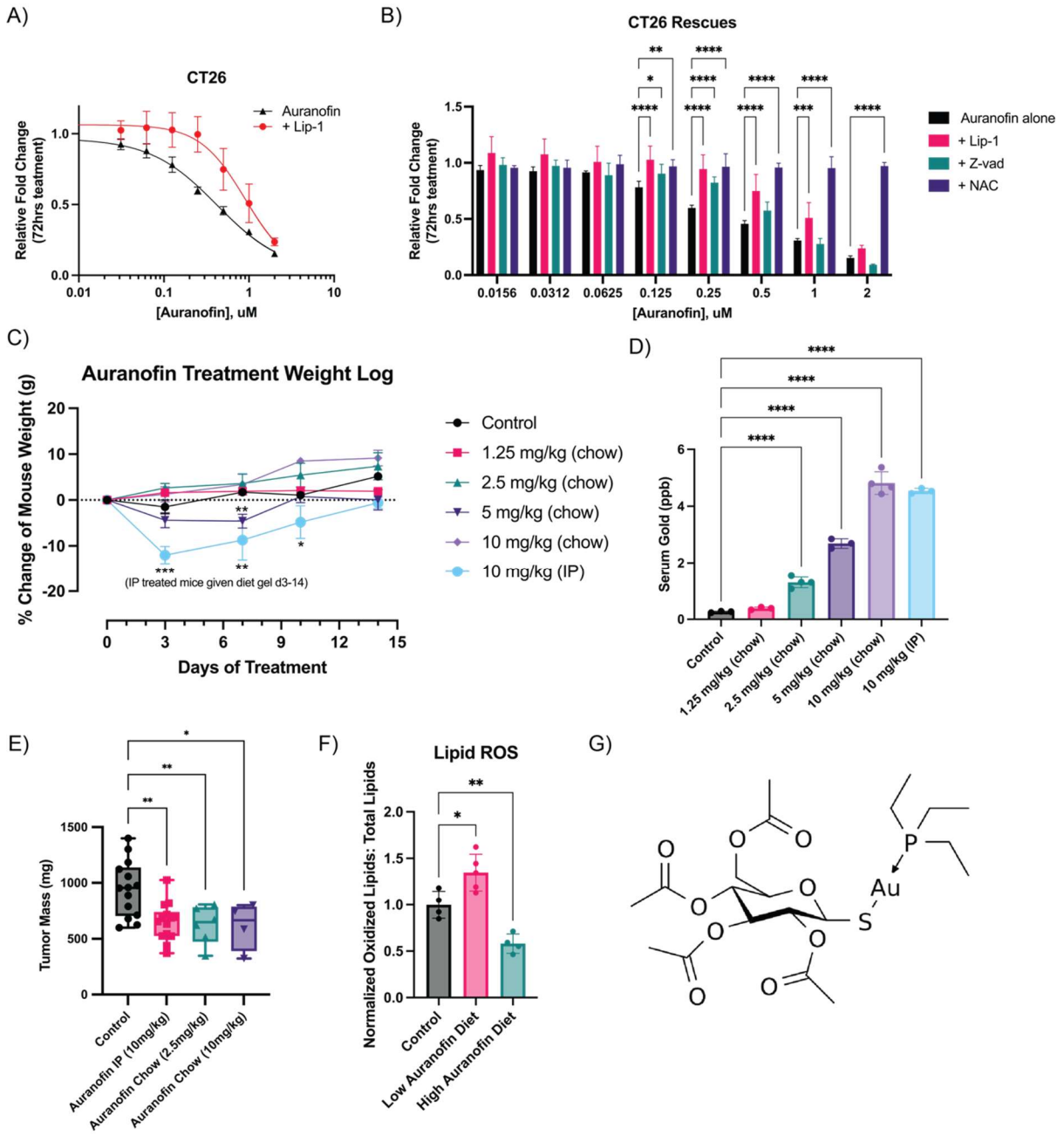

Figure S7

A) Live cell growth assay results of CT26 cells treated with Auranofin dose response +/- Lip-1 (1 μM) and normalized to untreated control. B) Full rescue panel quantification of CT26 cells treated with Auranofin dose response curve and rescue agents as indicated: Lip-1 (1 μM), Z-vad-FMK (10 μM), NAC (10 mM), Nec1 (10 μM). C) weight observations of auranofin treated mice, plotted as percent change normalized to weight at d0. D) ICPS measurements of gold levels in serum isolated from Auranofin treated mice. E) Composite data of all CT26 xenograft studies measuring final tumor mass. F) Lipid-ROS measurements of tumors from Auranofin chow studies, displayed as ratio of oxidized lipids:total lipids. G) Chemical structure of Auranofin
*: $p < 0.05$, **: $p < 0.01$, ***: $p < 0.001$, ****: $p < 0.0001$

References

1. Siegel, R. L., Giaquinto, A. N. & Jemal, A. Cancer statistics, 2024. *CA. Cancer J. Clin.* **74**, 12–49 (2024).
2. Rawla, P., Sunkara, T. & Barsouk, A. Epidemiology of colorectal cancer: incidence, mortality, survival, and risk factors. *Przegląd Gastroenterol.* **14**, 89–103 (2019).
3. Siegel, R. L., Wagle, N. S., Cercek, A., Smith, R. A. & Jemal, A. Colorectal cancer statistics, 2023. *CA. Cancer J. Clin.* **73**, 233–254 (2023).
4. Tomasetti, C., Marchionni, L., Nowak, M. A., Parmigiani, G. & Vogelstein, B. Only three driver gene mutations are required for the development of lung and colorectal cancers. *Proc. Natl. Acad. Sci.* **112**, 118–123 (2015).
5. Raskov, H., Søby, J. H., Troelsen, J., Bojesen, R. D. & Gögenur, I. Driver Gene Mutations and Epigenetics in Colorectal Cancer. *Ann. Surg.* **271**, 75 (2020).
6. Cercek, A. *et al.* PD-1 Blockade in Mismatch Repair-Deficient, Locally Advanced Rectal Cancer. *N. Engl. J. Med.* **386**, 2363–2376 (2022).
7. Jin, Z. & Sinicrope, F. A. Prognostic and Predictive Values of Mismatch Repair Deficiency in Non-Metastatic Colorectal Cancer. *Cancers* **13**, 300 (2021).
8. Dixon, S. J. *et al.* Ferroptosis: an iron-dependent form of nonapoptotic cell death. *Cell* **149**, 1060–1072 (2012).
9. Winterbourn, C. C. Toxicity of iron and hydrogen peroxide: the Fenton reaction. *Toxicol. Lett.* **82–83**, 969–974 (1995).
10. Jiang, X., Stockwell, B. R. & Conrad, M. Ferroptosis: mechanisms, biology and role in disease. *Nat. Rev. Mol. Cell Biol.* **22**, 266–282 (2021).
11. Chen, X., Comish, P. B., Tang, D. & Kang, R. Characteristics and Biomarkers of Ferroptosis. *Front. Cell Dev. Biol.* **9**, (2021).
12. Zilka, O. *et al.* On the Mechanism of Cytoprotection by Ferrostatin-1 and Liproxstatin-1 and the Role of Lipid Peroxidation in Ferroptotic Cell Death. *ACS Cent. Sci.* **3**, 232–243 (2017).

13. Yang, W. S. *et al.* Regulation of Ferroptotic Cancer Cell Death by GPX4. *Cell* **156**, 317–331 (2014).
14. Weaver, K. & Skouta, R. The Selenoprotein Glutathione Peroxidase 4: From Molecular Mechanisms to Novel Therapeutic Opportunities. *Biomedicines* **10**, 891 (2022).
15. Moghadaszadeh, B. & Beggs, A. H. Selenoproteins and Their Impact on Human Health Through Diverse Physiological Pathways. *Physiol. Bethesda Md* **21**, 307–315 (2006).
16. Labunskyy, V. M., Hatfield, D. L. & Gladyshev, V. N. Selenoproteins: molecular pathways and physiological roles. *Physiol. Rev.* **94**, 739–777 (2014).
17. Ingold, I. *et al.* Selenium Utilization by GPX4 Is Required to Prevent Hydroperoxide-Induced Ferroptosis. *Cell* **172**, 409-422.e21 (2018).
18. Sui, X. *et al.* RSL3 Drives Ferroptosis Through GPX4 Inactivation and ROS Production in Colorectal Cancer. *Front. Pharmacol.* **9**, 1371 (2018).
19. Győrffy, B. Transcriptome-level discovery of survival-associated biomarkers and therapy targets in non-small-cell lung cancer. *Br. J. Pharmacol.* **181**, 362–374 (2024).
20. Chandrashekar, D. S. *et al.* UALCAN: A Portal for Facilitating Tumor Subgroup Gene Expression and Survival Analyses. *Neoplasia N. Y. N* **19**, 649–658 (2017).
21. Chandrashekar, D. S. *et al.* UALCAN: An update to the integrated cancer data analysis platform. *Neoplasia N. Y. N* **25**, 18–27 (2022).
22. Wiederschain, D. *et al.* Single-vector inducible lentiviral RNAi system for oncology target validation. *Cell Cycle Georget. Tex* **8**, 498–504 (2009).
23. Huttlin, E. L. *et al.* A tissue-specific atlas of mouse protein phosphorylation and expression. *Cell* **143**, 1174–1189 (2010).
24. Liu, Q., Yin, X., Languino, L. R. & Altieri, D. C. Evaluation of drug combination effect using a Bliss independence dose-response surface model. *Stat. Biopharm. Res.* **10**, 112–122 (2018).

25. Skordos, I., Demeyer, A. & Beyaert, R. Analysis of T cells in mouse lymphoid tissue and blood with flow cytometry. *STAR Protoc.* **2**, 100351 (2021).
26. Bachmanov, A. A., Reed, D. R., Beauchamp, G. K. & Tordoff, M. G. Food Intake, Water Intake, and Drinking Spout Side Preference of 28 Mouse Strains. *Behav. Genet.* **32**, 435–443 (2002).
27. Cunniff, B., Snider, G. W., Fredette, N., Hondal, R. J. & Heintz, N. H. A direct and continuous assay for the determination of thioredoxin reductase activity in cell lysates. *Anal. Biochem.* **443**, 34–40 (2013).
28. Arnér, E. S. J., Zhong, L. & Holmgren, A. Preparation and assay of mammalian thioredoxin and thioredoxin reductase. in *Methods in Enzymology* vol. 300 226–239 (Academic Press, 1999).
29. Gheorghe, V. & Hart, T. Optimal construction of a functional interaction network from pooled library CRISPR fitness screens. *BMC Bioinformatics* **23**, 510 (2022).
30. Dolma, S., Lessnick, S. L., Hahn, W. C. & Stockwell, B. R. Identification of genotype-selective antitumor agents using synthetic lethal chemical screening in engineered human tumor cells. *Cancer Cell* **3**, 285–296 (2003).
31. Li, Z. *et al.* Ribosome stalling during selenoprotein translation exposes a ferroptosis vulnerability. *Nat. Chem. Biol.* **18**, 751–761 (2022).
32. Stockwell, B. R. *et al.* Ferroptosis: A Regulated Cell Death Nexus Linking Metabolism, Redox Biology, and Disease. *Cell* **171**, 273–285 (2017).
33. Weïwer, M. *et al.* Development of small-molecule probes that selectively kill cells induced to express mutant *RAS*. *Bioorg. Med. Chem. Lett.* **22**, 1822–1826 (2012).
34. Eaton, J. K. *et al.* Selective covalent targeting of GPX4 using masked nitrile-oxide electrophiles. *Nat. Chem. Biol.* **16**, 497–506 (2020).
35. Netto, L. E. S. & Antunes, F. The Roles of Peroxiredoxin and Thioredoxin in Hydrogen Peroxide Sensing and in Signal Transduction. *Mol. Cells* **39**, 65–71 (2016).

36. Stancill, J. S. & Corbett, J. A. The Role of Thioredoxin/Peroxiredoxin in the β-Cell Defense Against Oxidative Damage. *Front. Endocrinol.* **12**, 718235 (2021).
37. Cheff, D. M. *et al.* The ferroptosis inducing compounds RSL3 and ML162 are not direct inhibitors of GPX4 but of TXNRD1. *Redox Biol.* **62**, 102703 (2023).
38. Huang, F., Han, X., Xiao, X. & Zhou, J. Covalent Warheads Targeting Cysteine Residue: The Promising Approach in Drug Development. *Molecules* **27**, 7728 (2022).
39. Randolph, J. T. *et al.* Discovery of a Potent Chloroacetamide GPX4 Inhibitor with Bioavailability to Enable Target Engagement in Mice, a Potential Tool Compound for Inducing Ferroptosis In Vivo. *J. Med. Chem.* **66**, 3852–3865 (2023).
40. DeAngelo, S. L., Győrffy, B., Koutmos, M. & Shah, Y. M. Selenoproteins and tRNA-Sec: regulators of cancer redox homeostasis. *Trends Cancer* **9**, 1006–1018 (2023).
41. Glennås, A. *et al.* Auranofin is safe and superior to placebo in elderly-onset rheumatoid arthritis. *Br. J. Rheumatol.* **36**, 870–877 (1997).
42. Suarez-Almazor, M. E., Spooner, C., Belseck, E. & Shea, B. Auranofin versus placebo in rheumatoid arthritis. *Cochrane Database Syst. Rev.* **2000**, CD002048 (2000).
43. Pickering, I. J. *et al.* Direct Observation of Methylmercury and Auranofin Binding to Selenocysteine in Thioredoxin Reductase. *Inorg. Chem.* **59**, 2711–2718 (2020).
44. Dos Santos, H. F. Reactivity of auranofin with S-, Se- and N-containing amino acids. *Comput. Theor. Chem.* **1048**, 95–101 (2014).
45. Marzano, C. *et al.* Inhibition of thioredoxin reductase by auranofin induces apoptosis in cisplatin-resistant human ovarian cancer cells. *Free Radic. Biol. Med.* **42**, 872–881 (2007).
46. Fiskus, W. *et al.* Auranofin induces lethal oxidative and endoplasmic reticulum stress and exerts potent preclinical activity against chronic lymphocytic leukemia. *Cancer Res.* **74**, 2520–2532 (2014).

47. Bak, D. W., Gao, J., Wang, C. & Weerapana, E. A Quantitative Chemoproteomic Platform to Monitor Selenocysteine Reactivity within a Complex Proteome. *Cell Chem. Biol.* **25**, 1157-1167.e4 (2018).

48. Radenkovic, F., Holland, O., Vanderlelie, J. J. & Perkins, A. V. Selective inhibition of endogenous antioxidants with Auranofin causes mitochondrial oxidative stress which can be countered by selenium supplementation. *Biochem. Pharmacol.* **146**, 42–52 (2017).

49. Lamarche, J. *et al.* Mass spectrometry insights into interactions of selenoprotein P with auranofin and cisplatin. *J. Anal. At. Spectrom.* **37**, 1010–1022 (2022).

50. Zou, P. *et al.* Auranofin induces apoptosis by ROS-mediated ER stress and mitochondrial dysfunction and displayed synergistic lethality with piperlongumine in gastric cancer. *Oncotarget* **6**, 36505–36521 (2015).

51. Rano, T. A. *et al.* A combinatorial approach for determining protease specificities: Application to interleukin-1β converting enzyme (ICE). *Chem. Biol.* **4**, 149–155 (1997).

52. Schotte, P., Declercq, W., Van Huffel, S., Vandenabeele, P. & Beyaert, R. Non-specific effects of methyl ketone peptide inhibitors of caspases. *FEBS Lett.* **442**, 117–121 (1999).

53. Vandenabeele, P., Galluzzi, L., Vanden Berghe, T. & Kroemer, G. Molecular mechanisms of necroptosis: an ordered cellular explosion. *Nat. Rev. Mol. Cell Biol.* **11**, 700–714 (2010).

54. Endres, L. *et al.* Alkbh8 Regulates Selenocysteine-Protein Expression to Protect against Reactive Oxygen Species Damage. *PLoS ONE* **10**, e0131335 (2015).

55. Leonardi, A., Evke, S., Lee, M., Melendez, J. A. & Begley, T. J. Epitranscriptomic systems regulate the translation of reactive oxygen species detoxifying and disease linked selenoproteins. *Free Radic. Biol. Med.* **143**, 573–593 (2019).

56. Songe-Møller, L. *et al.* Mammalian ALKBH8 Possesses tRNA Methyltransferase Activity Required for the Biogenesis of Multiple Wobble Uridine Modifications Implicated in Translational Decoding. *Mol. Cell. Biol.* **30**, 1814–1827 (2010).

57. Fu, D. *et al.* Human AlkB homolog ABH8 Is a tRNA methyltransferase required for wobble uridine modification and DNA damage survival. *Mol. Cell. Biol.* **30**, 2449–2459 (2010).

58. Madhwani, K. R. *et al.* tRNA modification enzyme-dependent redox homeostasis regulates synapse formation and memory. *BioRxiv Prepr. Serv. Biol.* 2023.11.14.566895 (2023) doi:10.1101/2023.11.14.566895.

59. Lee, M. Y., Leonardi, A., Begley, T. J. & Melendez, J. A. Loss of epitranscriptomic control of selenocysteine utilization engages senescence and mitochondrial reprogramming. *Redox Biol.* **28**, 101375 (2020).

60. Lee, M. Y. *et al.* Selenoproteins and the senescence-associated epitranscriptome. *Exp. Biol. Med. Maywood NJ* **247**, 2090–2102 (2022).

61. Evke, S., Lin, Q., Melendez, J. A. & Begley, T. J. Epitranscriptomic Reprogramming Is Required to Prevent Stress and Damage from Acetaminophen. *Genes* **13**, 421 (2022).

62. van den Born, E. *et al.* ALKBH8-mediated formation of a novel diastereomeric pair of wobble nucleosides in mammalian tRNA. *Nat. Commun.* **2**, 172 (2011).

63. Blocka, K. L. N., Paulus, H. E. & Furst, D. E. Clinical Pharmacokinetics of Oral and Injectable Gold Compounds. *Clin. Pharmacokinet.* **11**, 133–143 (1986).

64. Capparelli, E. V., Bricker-Ford, R., Rogers, M. J., McKerrow, J. H. & Reed, S. L. Phase I Clinical Trial Results of Auranofin, a Novel Antiparasitic Agent. *Antimicrob. Agents Chemother.* **61**, e01947-16 (2017).